Towards monitoring the englacial fracture state using virtual-reflector seismology

Lindner, F.; Weemstra, C.; Walter, F.; Hadziioannou, C.

DOI
10.1093/gji/ggy156

Publication date
2018

Document Version
Final published version

Published in
Geophysical Journal International

Geophysical Journal International

Geophys. J. Int. (2018) **214,** 825–844
Advance Access publication 2018 April 19
GJI Seismology

doi: 10.1093/gji/ggy156

Towards monitoring the englacial fracture state using virtual-reflector seismology

F. Lindner,[1] C. Weemstra,[2,3] F. Walter[1] and C. Hadziioannou[4]

[1] *Laboratory of Hydraulics, Hydrology and Glaciology (VAW), ETH Zürich, Hönggerbergring 26, 8093 Zürich, Switzerland. E-mail: lindner@vaw.baug.ethz.ch*
[2] *Department of Geoscience and Engineering, Delft University of Technology, Stevinweg 1, 2628 CN Delft, The Netherlands*
[3] *Royal Netherlands Meteorological Institute, Utrechtseweg 297, 3731 GA De Bilt, The Netherlands*
[4] *Institute of Geophysics, Center for Earth System Research and Sustainability (CEN), Universität Hamburg, 20146 Hamburg, Germany*

Accepted 2018 April 18. Received 2018 March 22; in original form 2017 November 15

SUMMARY

In seismology, coda wave interferometry (CWI) is an effective tool to monitor time-lapse changes using later arriving, multiply scattered coda waves. Typically, CWI relies on an estimate of the medium's impulse response. The latter is retrieved through simple time-averaging of receiver-receiver cross-correlations of the ambient field, that is, seismic interferometry (SI). In general, the coda is induced by heterogeneities in the Earth. Being comparatively homogeneous, however, ice bodies such as glaciers and ice sheets exhibit little scattering. In addition, the temporal stability of the time-averaged cross-correlations suffers from temporal variations in the distribution and amplitude of the passive seismic sources. Consequently, application of CWI to ice bodies is currently limited. Nevertheless, fracturing and changes in the englacial macroscopic water content alter the bulk elastic properties of ice bodies, which can be monitored with cryoseismological measurements. To overcome the current limited applicability of CWI to ice bodies, we therefore introduce virtual-reflector seismology (VRS). VRS relies on a so-called multidimensional deconvolution (MDD) process of the time-averaged cross-correlations. The technique results in the retrieval of a medium response that includes virtual reflections from a contour of receivers enclosing the region of interest (i.e. the region to be monitored). The virtual reflections can be interpreted as artificial coda replacing the (lacking) natural scattered coda. Hence, this artificial coda might be exploited for the purpose of CWI. From an implementation point of view, VRS is similar to SI by MDD, which, as its name suggests, also relies on a multidimensional deconvolution process. SI by MDD, however, does not generate additional virtual reflections. Advantageously, both techniques mitigate spurious coda changes associated with temporal variations in the distribution and amplitude of the passive seismic sources. In this work, we apply SI by MDD and VRS to synthetic and active seismic surface-wave data. The active seismic data were acquired on Glacier de la Plaine Morte, Switzerland. We successfully retrieve virtual reflections through the application of VRS to this active seismic data. In application to both synthetic and active seismic data, we show the potential of VRS to monitor time-lapse changes. In addition, we find that SI by MDD allows for a more accurate determination of phase velocity.

Key words: Seismic interferometry; Glaciology; Coda waves; Wave scattering and diffraction; Fracture and flow.

1 INTRODUCTION

Changes in elastic material properties affect seismic wave propagation. In particular, changes in these properties may lead to changes in seismic velocities. Applied to earthquake seismology, Poupinet *et al.* (1984) used repeating earthquakes, called 'doublets', to observe such small velocity changes, which they attributed to crustal elasticity changes. More recently, seismologists used virtual-source responses retrieved through the application of seismic interferometry (SI) for this purpose (Sens-Schönfelder & Wegler 2006; Brenguier *et al.* 2008; Mordret *et al.* 2016). Classically, SI turns one of a pair of seismic receivers into a virtual source through a simple cross-correlation of ground motion recordings. The response to this virtual source is retrieved at the location of the other receiver

(Shapiro & Campillo 2004; Bakulin & Calvert 2006). We refer to this conventional approach as SI by cross-correlation (SI by CC). Under the condition that the medium is both lossless and illuminated uniformly from all directions, the retrieved response can be related to the elastic Green's function between the two receiver locations (Wapenaar & Fokkema 2006). In practice, ambient noise vibrations (e.g. Shapiro & Campillo 2004), earthquake recordings (e.g. Campillo 2003) and active shot data (e.g. Schuster *et al.* 2004) can be used for the cross-correlation of station pair signals to retrieve an estimate of the medium's impulse response.

Repeated retrieval of interstation impulse responses through the application of SI to recordings of the ambient seismic field can replace the earthquake doublets used by Poupinet *et al.* (1984). This may allow monitoring of subsurface velocity changes smaller than half a per cent and with a daily resolution (Sens-Schönfelder & Wegler 2006; Obermann *et al.* 2014). Usually, the measurement of velocity changes relies on later arriving coda waves of ambient-field derived medium responses, which have followed an indirect and thus longer path through the medium. This indirect path can be the result of scattering off heterogeneities in the medium, but can also result from multiple reflections or reverberations, as outlined in Grêt *et al.* (2006). As the coda waves propagate through the medium, they sample the same volume more densely, which renders them more sensitive to small velocity changes (Snieder *et al.* 2002). In seismology, typically the coda is assumed to consist mainly of waves scattered by crustal heterogeneities (Aki & Chouet 1975). However, in laboratory settings, studies of small velocity changes have relied on coda arising from reverberations and reflections off boundaries (Lobkis & Weaver 2003).

One of the prerequisites for SI by CC is a stable, uniform angular distribution of sources, thus ensuring even illumination from all directions (e.g. Gouedard *et al.* 2008). The effect of a non-uniform illumination has been investigated in theoretical studies by, for example, Tsai (2009), Weaver *et al.* (2009) and Halliday & Curtis (2008). They have shown that a non-uniform distribution of sources with angle can result in a bias on the direct arrivals in the resulting noise correlation function. Using field data, Froment *et al.* (2010) confirmed the presence of such phase shifts on ballistic waves predicted by Weaver *et al.* (2009). Since imaging studies typically use these direct arrivals to estimate seismic wave traveltimes, these phase shifts can induce errors, as discussed in Yang & Ritzwoller (2008) and Yao & van der Hilst (2009). As pointed out by van Wijk *et al.* (2011), however, these issues may be mitigated also by utilizing cross-component cross-correlations besides the typically used vertical-vertical cross-correlations, since these are less affected by irregularities in the illumination pattern (Xu & Mikesell 2017). In contrast to the ballistic wave arrival, Froment *et al.* (2010) have shown that the later arriving coda waves are almost unaffected by an anisotropic illumination pattern, as scattering homogenizes the wavefield. This is an advantage in monitoring applications, where the use of coda waves renders any spatial anisotropy of the noise field less problematic (Hadziioannou *et al.* 2009). In case of a time-varying illumination pattern, Colombi *et al.* (2014) present an estimate of the small errors on wave speed variations. Besides a time-varying illumination pattern, Zhan *et al.* (2013) show that temporal changes in the frequency content of the illuminating wavefield can introduce errors in the velocity variations measured from coda.

In recent years, a different type of SI, namely SI by multidimensional deconvolution (SI by MDD), has been introduced (Wapenaar & van der Neut 2010; Wapenaar *et al.* 2011b). In this formulation, the responses obtained from SI by CC are deconvolved by a so-called point-spread function (PSF). This PSF quantifies the illumination pattern using recordings by a set of additional receivers along a contour through the virtual-source's location. By means of a multidimensional deconvolution process, the imprint of the (non-uniform) illumination pattern can then be removed from the CC responses. Thus, SI by MDD relaxes the conditions associated with SI by CC and improves the quality of the retrieved medium responses (van der Neut *et al.* 2011; Wapenaar *et al.* 2011b). Most notably, SI by MDD does not require the medium to be lossless and corrects the deviation of the cross-correlation responses from the medium's Green's function. The latter correction implies that SI by MDD renders the SI by CC requirement of a uniform illumination pattern unnecessary. Recently, van Dalen *et al.* (2015) and Weemstra *et al.* (2017a) applied SI by MDD to ambient noise surface-wave data. Both studies conclude that the phase of the retrieved responses is corrected for inaccuracies arising from a non-uniform illumination of the medium. In other words, the retrieval of virtual-source responses through SI by MDD does not rely on a uniform illumination pattern. For monitoring purposes, this implies that, with respect to the application of SI by CC, the temporal resolution might be increased through the application of SI by MDD (Weemstra *et al.* 2017a).

SI by MDD has the additional advantage that a reflecting boundary condition may be imposed on the receiver contour used for SI by MDD (Weemstra *et al.* 2015b). In case of an appropriate receiver contour (partly) enclosing the medium of interest, the reflecting boundary condition gives rise to virtual reflections from the receiver contour. This approach, hereafter termed virtual-reflector seismology (VRS), creates an artificial reflection coda, which might be used for coda wave interferometry (CWI) in order to measure small velocity changes. In particular, VRS is an attractive choice for monitoring applications in media with little scattering. In that case, the reflection coda takes the place of the (lacking) naturally scattered coda. The repeated sampling of the medium by the reverberating virtual reflections is expected to increase the detectability of small velocity variations.

The perspective to monitor small medium changes despite limited scattering makes VRS attractive for the study of ice bodies such as glaciers, ice sheets and ice shelves. Whereas glacial ice is rather homogeneous, even under common conditions, gravity-driven ice flow, ice–water interaction and basal friction force the ice, resulting in some degree of brittle failure. At the surface of an ice body, brittle failure often becomes visible by crevassing (Colgan *et al.* 2015), iceberg calving (Benn *et al.* 2007) or rifting (e.g. Fricker *et al.* 2005; Bassis *et al.* 2008). It may, however, also occur on smaller scales englacially below the penetration depth of crevasses (Deichmann & Röthlisberger 1979; Van der Veen 1998; Walter *et al.* 2009). Fracturing radiates seismic waves, which have been studied for decades (e.g. Neave & Savage 1970; Lawrence & Qamar 1979), and these events ('icequakes') demonstrate that the ice bulk is constantly subject to structural changes (e.g. Walter *et al.* 2009). The consequences of such fracturing-induced medium changes are far reaching and include the release of huge icebergs into the ocean (Joughin & MacAyeal 2005; Amundson *et al.* 2008), the break-up of ice shelfs (Rott *et al.* 1996; Scambos *et al.* 2003), ice avalanching (Huggel *et al.* 2005) and the sudden drainage of glacier-dammed lakes (Roberts 2005; Das *et al.* 2008). Especially, the latter two are a severe threat to human settlements (e.g. Richardson & Reynolds 2000; Jain *et al.* 2012). Additionally, crevassing increases the ice damage state (Pralong & Funk 2005) and favours cryohydrologic warming and thus ice softening (Phillips *et al.* 2010; Colgan *et al.* 2015). Besides fracturing, the medium properties might be altered

Table 1. Acronyms used in this study.

Acronym	Meaning
CWI	Coda-wave interferometry
SI by CC	Seismic interferometry by cross-correlation
SI by MDD	Seismic interferometry by multidimensional deconvolution
VRS	Virtual-reflector seismology
CCF	Cross-correlation function; defined in eq. (2)
PSF	Point-spread function; defined in eq. (7)

by changing water content of void spaces on daily to seasonal scales (e.g. Fountain & Walder 1998). Primarily, the water content in ice bodies is of interest since the subglacial hydraulic system strongly influences basal ice flow (e.g. Iken & Bindschadler 1986; Clarke 2005).

In order to measure englacial structural changes, Walter *et al.* (2015) investigated a monitoring scheme for alpine glaciers applying SI by CC to icequake data. However, these authors conclude that limited englacial scattering makes the approach of CWI an unattractive choice for monitoring englacial changes. Additionally, variable icequake source locations both in space and time (e.g. Roux *et al.* 2010) complicate the retrieval of stable virtual-source responses.

To overcome these limitations of SI by CC encountered in glaciology, we test the applicability of SI by MDD and VRS to synthetic data and active-source seismic data acquired on an alpine glacier. We first review the theories underlying SI by CC, SI by MDD and VRS (Table 1 lists all acronyms used in this study for better readability). Additionally, we recapitulate the methods for phase velocity retrieval from interferometric responses and matched-field processing. Subsequently, we apply the theories to synthetic acoustic data and active-source seismic data acquired on Glacier de la Plaine Morte, Switzerland. The active sources allow a controlled experiment environment suitable for testing different concepts. In principle, the hammer blows can be replaced by frequently occurring (several hundreds per day) shallow icequakes whose simple waveforms allow for efficient and automatic location (Roux *et al.* 2010). This eliminates the need for an active source. Our first application investigates monitoring perspectives of SI by MDD and VRS. In a second application, based on the work of Aki (1957) and Ekström *et al.* (2009), we compare phase velocity dispersion curves extracted from medium responses retrieved through the application of SI by CC and SI by MDD. In addition, as a quality check, we compare the recovered glacial dispersion curve to the dispersion curve extracted using matched-field processing.

2 THEORY

In this study, we test the suitability of SI by MDD and VRS for the purpose of englacial monitoring. In particular, we focus on the application of these techniques to glacial surface waves excited at the glacier's surface. Assuming single-mode dispersive surface waves, we may restrict our discussion to scalar waves propagating through a 2-D homogeneous medium (e.g. Tsai 2011). For example, Wapenaar *et al.* (2011a) use the scalar formulation to showcase the benefit of SI by MDD over SI by CC for the purpose of surface-wave retrieval using USArray station locations. In case multiple (strong) surface-wave modes exist, however, the scalar formulation is not directly applicable. This can be attributed to non-vanishing cross-modal terms, which result from the fact that the orthogonality of the different modes is not fulfilled (Halliday & Curtis 2008; Kimman & Trampert 2010; van Dalen *et al.* 2014). In that case, mode separation will be required prior to Green's function retrieval (irrespective of whether that will be done using SI by CC, SI by MDD or VRS), such that interferometric Green's functions can be retrieved for each mode individually.

In our glacier experiment, active seismic sources are used: signal is generated by a stroke of a sledgehammer on a metal plate, which is placed on the surface of the glacier. The rapid deceleration of the sledgehammer hitting the metal plate exerts a large downward force, which we consider a point source. The glacier's response to this point source is measured by three-component geophones and the measured quantity is particle velocity. We restrict our analysis to vertical-component (x_3) surface-wave recordings, which, considering a laterally invariant medium, effectively behave as scalar waves travelling in the surface (x_1, x_2) plane. Most of the (interferometric) relations introduced below are frequency dependent: frequency dependency of a variable is indicated by a hat, for example, $\hat{f} \equiv \hat{f}(\omega)$.

Using the Fourier convention $\hat{f}(\omega) = \frac{1}{\sqrt{2\pi}} \int_{-\infty}^{\infty} f(t) e^{-i\omega t}\, \mathrm{d}t$, the Green's function for vertical particle velocity at $\boldsymbol{x}_\mathrm{R}$ (in this work, vectors and matrices are indicated in bold) due to a vertical impulsive point source at $\boldsymbol{x}_\mathrm{S}$ reads (Aki & Richards 2002; van Dalen *et al.* 2014)

$$\hat{G}\left(\boldsymbol{x}_\mathrm{R}, \boldsymbol{x}_\mathrm{S}\right) = \frac{\omega}{4\hat{A}\hat{c}} H_0^{(2)}\left(\hat{k}\left|\boldsymbol{x}_\mathrm{R} - \boldsymbol{x}_\mathrm{S}\right|\right). \tag{1}$$

Here, ω denotes angular frequency, $\hat{c}$ the Rayleigh wave's frequency-dependent phase velocity and $\hat{k}$ the frequency-dependent wavenumber, which, in a lossless medium, coincides with $\omega/\hat{c}$. The function $H_0^{(2)}$ is a zeroth-order Hankel function of the second kind. Note that the (far-field) expressions in Aki & Richards (2002) and van Dalen *et al.* (2014) are multiplied by a factor $i\omega$ (i being the imaginary unit) to obtain the Green's function above (those authors consider particle displacement). Since both receivers and sources are located at the glacier's surface, all locations are uniquely defined by their x_1 and x_2 coordinates, that is, $\boldsymbol{x}_\mathrm{R} \equiv (x_{\mathrm{R}_1}, x_{\mathrm{R}_2})$ and $\boldsymbol{x}_\mathrm{S} \equiv (x_{\mathrm{S}_1}, x_{\mathrm{S}_2})$. Furthermore, we refer to $\hat{A}$ as a frequency-dependent modal scale factor. In our case (vertical particle velocity recorded by surface receivers due to vertically polarized surface sources), $\hat{A} \equiv 2\hat{U}\boldsymbol{I}_1 / r_2^2(0)$, where $\hat{U}$ is the (frequency-dependent) Rayleigh wave's group velocity, $\boldsymbol{I}_1$ its modal kinetic energy and $r_2(0)$ the value of the modal eigenfunction at the surface ($x_3 = 0$). Note that this modal scale factor is always positive. It should be understood that the vertical particle velocity described by eq. (1) is limited to a single surface-wave mode.

In anticipation of the interferometric theory introduced below, let us define the cross-correlation function (CCF)

$$\hat{C}\left(\boldsymbol{x}_\mathrm{R}, \boldsymbol{x}\right) \equiv \sum_j \hat{v}\left(\boldsymbol{x}_\mathrm{R}, \boldsymbol{x}_\mathrm{S}^{(j)}\right) \hat{v}^*\left(\boldsymbol{x}, \boldsymbol{x}_\mathrm{S}^{(j)}\right), \tag{2}$$

where $\hat{v}\left(\boldsymbol{x}_\mathrm{R}, \boldsymbol{x}_\mathrm{S}^{(j)}\right)$ and $\hat{v}\left(\boldsymbol{x}, \boldsymbol{x}_\mathrm{S}^{(j)}\right)$ represent recordings of vertical-component particle velocity at $\boldsymbol{x}_\mathrm{R}$ and $\boldsymbol{x}$, respectively, due to a vertical point source at $\boldsymbol{x}_\mathrm{S}^{(j)}$. The asterisk in eq. (2) denotes complex conjugation and hence the products on the right-hand side correspond to cross-correlations in the time domain. Furthermore, a recording $\hat{v}\left(\boldsymbol{x}_\mathrm{R}, \boldsymbol{x}_\mathrm{S}^{(j)}\right)$ is defined as $\hat{v}\left(\boldsymbol{x}_\mathrm{R}, \boldsymbol{x}_\mathrm{S}^{(j)}\right) \equiv \hat{G}\left(\boldsymbol{x}_\mathrm{R}, \boldsymbol{x}_\mathrm{S}^{(j)}\right) \hat{s}\left(\boldsymbol{x}_\mathrm{S}^{(j)}\right)$, where $\hat{s}\left(\boldsymbol{x}_\mathrm{S}^{(j)}\right)$ is the spectrum of the signal emitted by the source at $\boldsymbol{x}_\mathrm{S}^{(j)}$; the same holds for $\hat{v}\left(\boldsymbol{x}, \boldsymbol{x}_\mathrm{S}^{(j)}\right)$. Finally, we should note that we do not (yet) associate eq. (2) with a specific source and/or receiver configuration.

Below, we briefly revisit the theory underlying SI by CC, SI by MDD and VRS (Sections 2.1, 2.2 and 2.3, respectively). All

three techniques allow the retrieval of a medium's virtual-source response. They are, however, subject to different conditions. In particular, this concerns the illumination pattern and receiver geometry (Wapenaar *et al.* 2011b; Weemstra *et al.* 2017b). SI by CC is most restrictive in terms of medium properties and illumination. SI by MDD and VRS are less restrictive, but are technically more involved and have greater requirements concerning receiver geometry. Provided these requirements are met, however, these two techniques allow the retrieval of more accurate medium responses (Wapenaar *et al.* 2011b; Weemstra *et al.* 2017a). After introducing the interferometric formulations, we explain in Section 2.4 how surface-wave phase velocities can be extracted from the retrieved responses, and introduce in Section 2.5 the theory underlying our matched-field processing approach, which we also use for phase velocity extraction.

2.1 SI by cross-correlation

Consider the configuration in Fig. 1(a) (top). Assuming equally powerful, band-limited sources, the CCF computed from the recordings at $\boldsymbol{x}$ and $\boldsymbol{x}_\mathrm{R}$ can be related to the impulse response between these two locations (e.g. Boschi & Weemstra 2015). Specifically, both the band-limited Green's function between $\boldsymbol{x}$ and $\boldsymbol{x}_\mathrm{R}$, and its time reverse, can be retrieved. In application to Rayleigh waves, this reads (Halliday & Curtis 2008),

$$\hat{C}\left(\boldsymbol{x}_\mathrm{R},\boldsymbol{x}\right) = \frac{1}{\hat{A}}\left[\hat{G}\left(\boldsymbol{x}_\mathrm{R},\boldsymbol{x}\right)+\hat{G}^{*}\left(\boldsymbol{x}_\mathrm{R},\boldsymbol{x}\right)\right]\hat{S}, \tag{3}$$

where $\hat{S}$ denotes the power spectrum of the sources, including an implicit normalization dependent on the density of the discrete sources (e.g. Weemstra *et al.* 2014). Here, $\hat{S}$ does not depend on $\boldsymbol{x}_\mathrm{S}$, because eq. (3) is derived assuming (i) equally powerful sources (i.e. for a total of N sources, $\hat{s}\left(\boldsymbol{x}_\mathrm{S}^{(1)}\right)\hat{s}^{*}\left(\boldsymbol{x}_\mathrm{S}^{(1)}\right)=\hat{s}\left(\boldsymbol{x}_\mathrm{S}^{(2)}\right)\hat{s}^{*}\left(\boldsymbol{x}_\mathrm{S}^{(2)}\right)=\cdots=\hat{s}\left(\boldsymbol{x}_\mathrm{S}^{(N)}\right)\hat{s}^{*}\left(\boldsymbol{x}_\mathrm{S}^{(N)}\right)$), and (ii) that the density of these sources does not vary as a function of azimuth [see Fig. 1(a)]. It is useful to note that in case sources are simultaneously acting uncorrelated noise sources, instead of sequentially acting active sources, the explicit summation over sources is obviated. The summation in eq. (2) may, in that case, be replaced by integration over sufficiently long time and/or summation over sufficient cross-correlation windows (e.g. Shapiro & Campillo 2004; Wapenaar & Fokkema 2006).

The inverse Fourier transform of $\hat{G}\left(\boldsymbol{x}_\mathrm{R},\boldsymbol{x}\right)+\hat{G}^{*}\left(\boldsymbol{x}_\mathrm{R},\boldsymbol{x}\right)$ reads $G\left(\boldsymbol{x}_\mathrm{R},\boldsymbol{x},t\right)+G\left(\boldsymbol{x}_\mathrm{R},\boldsymbol{x},-t\right)$. Anticipating the introduction of SI by MDD in Section 2.2, let us consider the so-called stationary-phase points associated with $G\left(\boldsymbol{x}_\mathrm{R},\boldsymbol{x},t\right)$ and $G\left(\boldsymbol{x}_\mathrm{R},\boldsymbol{x},-t\right)$ (e.g. Arfken & Weber 2005). For our laterally invariant medium and the circular distribution of sources in Fig. 1(a), these stationary-phase points are the points where the circular source distribution intersects with the line connecting $\boldsymbol{x}$ and $\boldsymbol{x}_\mathrm{R}$ (e.g. Snieder 2004). The dominant contribution to the summation in eq. (2) comes from these stationary-phase points. To facilitate comparison with SI by MDD, we consider the receivers at $\boldsymbol{x}$ and $\boldsymbol{x}_\mathrm{R}$ to be illuminated by sources located on a half-circle, instead of a full circle. In particular, we consider that half circle to include the so-called stationary-phase point associated with $G\left(\boldsymbol{x}_\mathrm{R},\boldsymbol{x},t\right)$, but to exclude the stationary-phase point associated with $G\left(\boldsymbol{x}_\mathrm{R},\boldsymbol{x},-t\right)$. For the configuration in Fig. 1(a), this can be achieved by summing only cross-correlations due to sources along the upper half-circle. Ignoring artefacts due to the truncation of the source distribution (e.g. Snieder *et al.* 2008), this implies that

$$\hat{C}\left(\boldsymbol{x}_\mathrm{R},\boldsymbol{x}\right) = \frac{1}{\hat{A}}\hat{G}\left(\boldsymbol{x}_\mathrm{R},\boldsymbol{x}\right)\hat{S}. \tag{4}$$

The relation between the Green's function and the CCF in eqs (3) and (4) is quite accurate in case the medium is lossless and the (half)-circular contour along which the sources are placed is located at large distance (Wapenaar & Fokkema 2006). As such, it allows one to retrieve an estimate of a medium's Green's function (e.g. Mikesell *et al.* 2012; Weemstra *et al.* 2013). In many practical applications, however, the medium is not lossless. Moreover, active sources can, in practice, not always be located such that they span an enclosing boundary (e.g. Halliday *et al.* 2008). In addition, variations in coupling between the active sources and the underlying medium may effectively result in a non-uniform illumination. In application to the passive data, the inherent lack of control over the location and strength of the passive sources often also results in a non-uniform illumination pattern (e.g. Walter *et al.* 2015; Chang *et al.* 2016). Dissipation of energy and/or deviation from a uniform illumination pattern degrade the accuracy of the retrieved Green's functions and may result in erroneous estimates of phase velocity (e.g. Tsai 2009; Weaver *et al.* 2009). Also, a time-varying illumination pattern may result in temporal variations in the coda of the retrieved virtual-source responses. Such variations may obscure coda variations associated with structural changes in the medium, and may hence limit monitoring capabilities (e.g. Lehujeur *et al.* 2015; Weemstra *et al.* 2016). Taken all together, SI by CC is, strictly speaking, therefore rather restrictive in terms of medium properties and illumination. SI by MDD and VRS circumvent some of the limitations inherent in SI by CC, and, as such, allow the retrieval of more accurate medium responses (Wapenaar *et al.* 2011b; Weemstra *et al.* 2017b).

2.2 SI by multidimensional deconvolution

Whereas eqs (3) and (4) are derived from a correlation-type Green's function representation, the formulation underlying SI by MDD is derived from a convolution-type Green's function representation (Wapenaar & van der Neut 2010; van Dalen *et al.* 2014). Consequently, contrary to SI by CC, successful application of SI by MDD does not require the medium to be lossless. Moreover, SI by MDD permits illumination-related deviations of the (source-averaged) cross-correlation from the medium's actual Green's function to be corrected. Let us, therefore, consider the configuration in Fig. 1(b) (top), where the receiver at $\boldsymbol{x}_\mathrm{R}$ is illuminated from one side by non-uniformly distributed sources. The location of source number j is given by $\boldsymbol{x}_\mathrm{S}^{(j)}$ and the different sources may vary in power. Assuming receivers at $\boldsymbol{x}'$ along a smooth contour $\mathbb{S}_\mathrm{rec}$ that separates the region containing the sources from the region in which $\boldsymbol{x}_\mathrm{R}$ is located, it can be shown that for each of the sources (van Dalen *et al.* 2014),

$$\hat{v}\left(\boldsymbol{x}_\mathrm{R},\boldsymbol{x}_\mathrm{S}^{(j)}\right) = 2\hat{A}\int_{\mathbb{S}_\mathrm{rec}}\hat{\tilde{G}}_\mathrm{d}^{(\mathrm{a})}\left(\boldsymbol{x}_\mathrm{R},\boldsymbol{x}'\right)\hat{v}\left(\boldsymbol{x}',\boldsymbol{x}_\mathrm{S}^{(j)}\right)\mathrm{d}\boldsymbol{x}'. \tag{5}$$

Here, the subscript d denotes that $\hat{\tilde{G}}_\mathrm{d}^{(\mathrm{a})}$ is a so-called dipole Green's function. For vertical particle velocity associated with a single-mode dispersive surface wave, this dipole Green's function is defined as $\hat{\tilde{G}}_\mathrm{d}^{(\mathrm{a})}\left(\boldsymbol{x}_\mathrm{R},\boldsymbol{x}'\right)\equiv\left[i\hat{c}/\omega\right]\nabla\hat{\tilde{G}}^{(\mathrm{a})}\left(\boldsymbol{x}_\mathrm{R},\boldsymbol{x}'\right)\cdot\boldsymbol{n}$, where the 2-D spatial derivative of $\hat{\tilde{G}}^{(\mathrm{a})}\left(\boldsymbol{x}_\mathrm{R},\boldsymbol{x}'\right)$ is computed at $\boldsymbol{x}'$ along $\mathbb{S}_\mathrm{rec}$, and $\boldsymbol{n}=(n_1,n_2)$ is the outward pointing normal vector. By employing a stationary phase approximation, van Dalen *et al.* (2014) show that

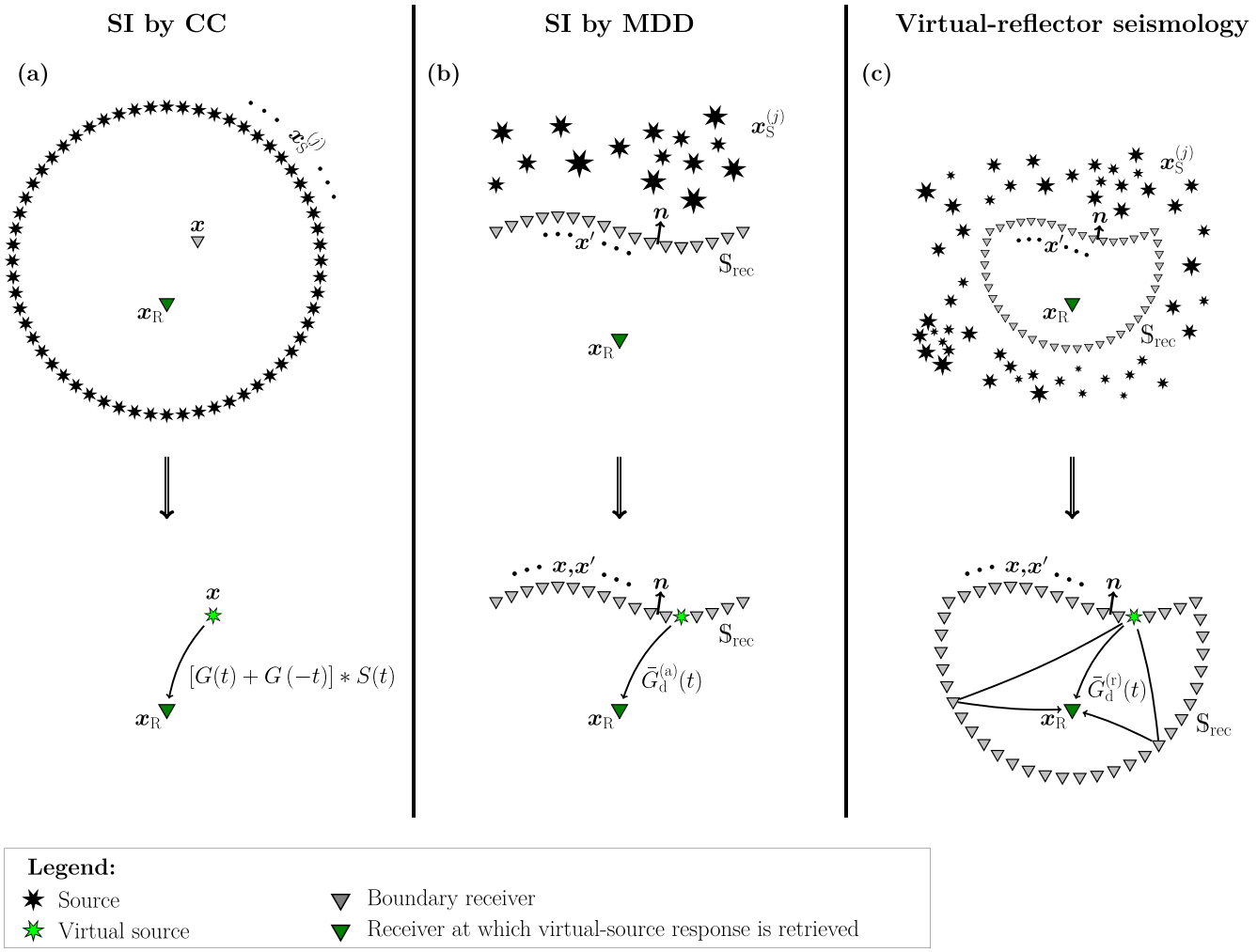

Figure 1. (a) Configuration associated with SI by CC, that is, eq. (3). The receivers can be turned into perfect virtual sources if illuminated uniformly from all angles. Note that $[G(\boldsymbol{x}_{\mathrm{R}},\boldsymbol{x},t)+G(\boldsymbol{x}_{\mathrm{R}},\boldsymbol{x},-t)]*S(t)$ is the inverse Fourier transform of $\left[\hat{G}(\boldsymbol{x}_{\mathrm{R}},\boldsymbol{x})+\hat{G}^{*}(\boldsymbol{x}_{\mathrm{R}},\boldsymbol{x})\right]\hat{S}$, where the in-line asterisk denotes temporal convolution. (b) Configuration associated with SI by MDD, that is, eqs (5) and (6). The variation in both density and size of the depicted sources manifests that the one-sided illumination does not need to be uniform in this case. Non-uniformities in the illumination pattern are captured by the receiver boundary and encoded in the PSF. Subsequent multidimensional deconvolution of the CCF with the PSF corrects the virtual-source responses for the accrued artefacts (note that $\bar{G}_{\mathrm{d}}^{(\mathrm{a})}(t)$ is the inverse Fourier transform of $\hat{\bar{G}}_{\mathrm{d}}^{(\mathrm{a})}$). (c) Configuration associated with VRS, that is, eqs (8) and (10). Again, the variation in density and size of the depicted sources manifests that the (in this case omnidirectional) illumination of the region of interest does not need to be uniform. The additional ray paths indicate virtual reflections from the receiver boundary (note that $\bar{G}_{\mathrm{d}}^{(\mathrm{r})}(t)$ is the inverse Fourier transform of $\hat{\bar{G}}_{\mathrm{d}}^{(\mathrm{r})}$).

$\nabla\hat{\bar{G}}^{(\mathrm{a})}(\boldsymbol{x}_{\mathrm{R}},\boldsymbol{x}')\cdot\boldsymbol{n}$ can be approximated by $-i\hat{k}\hat{\bar{G}}^{(\mathrm{a})}(\boldsymbol{x}_{\mathrm{R}},\boldsymbol{x}')$ in case $\hat{k}\,|\boldsymbol{x}_{\mathrm{R}}-\boldsymbol{x}'|\gg 1$.

The sought-for dipole Green's function $\hat{\bar{G}}_{\mathrm{d}}^{(\mathrm{a})}(\boldsymbol{x}_{\mathrm{R}},\boldsymbol{x}')$ is associated with a so-called reference medium (hence the bar), whereas, $\hat{v}\left(\boldsymbol{x}_{\mathrm{R}},\boldsymbol{x}_{\mathrm{S}}^{(j)}\right)$ and $\hat{v}\left(\boldsymbol{x}',\boldsymbol{x}_{\mathrm{S}}^{(j)}\right)$ are associated with the actual medium, that is, the field recordings. The reference medium coincides with the actual medium in the region of interest (i.e. the region on the side of $\mathbb{S}_{\mathrm{rec}}$ that contains $\boldsymbol{x}_{\mathrm{R}}$), but may have different medium parameters outside $\mathbb{S}_{\mathrm{rec}}$ (Wapenaar & van der Neut 2010). Eq. (5) is derived assuming absorbing boundary conditions along $\mathbb{S}_{\mathrm{rec}}$ in this reference medium (Wapenaar *et al.* 2011b; Weemstra *et al.* 2017b). Anticipating the introduction of VRS in the next section, the absorbing nature of the reference medium is explicitly indicated by means of the superscript (a). The absorbing boundary conditions also imply that eq. (5) only holds for waves propagating in one direction across $\mathbb{S}_{\mathrm{rec}}$, that is, waves traversing $\mathbb{S}_{\mathrm{rec}}$ from the region containing the $\boldsymbol{x}_{\mathrm{S}}^{(j)}$ into the region containing $\boldsymbol{x}_{\mathrm{R}}$. Consequently, eq. (5) does not apply to source configurations where signal is excited on the same side of $\mathbb{S}_{\mathrm{rec}}$ as $\boldsymbol{x}_{\mathrm{R}}$. Also, the condition implies that, without explicit wavefield separation along $\mathbb{S}_{\mathrm{rec}}$, SI by MDD is only applicable to configurations where the medium is illuminated from a single side (Wapenaar & van der Neut 2010) and where no energy scatters back through $\mathbb{S}_{\mathrm{rec}}$. For single-mode surface waves propagating through a laterally invariant medium, and a configuration where the sources at $\boldsymbol{x}_{\mathrm{S}}^{(j)}$ and the receiver at $\boldsymbol{x}_{\mathrm{R}}$ are located on opposite sides of $\mathbb{S}_{rec}$, this condition is fulfilled.

Eq. (5) holds for each $\boldsymbol{x}_{\mathrm{S}}^{(j)}$ individually, effectively yielding a set of equations. Solving this set of equations for $\hat{\bar{G}}_{\mathrm{d}}^{(\mathrm{a})}$, including $2\hat{A}$ in our case, is what is referred to as SI by MDD in this work. This can be accomplished, for example, in a least-squares sense: introducing the auxiliary variable $\boldsymbol{x}$ along $\mathbb{S}_{\mathrm{rec}}$ (see Fig. 1b, bottom) and multiplying both sides of eq. (5) with $\hat{v}^{*}\left(\boldsymbol{x},\boldsymbol{x}_{\mathrm{S}}^{(j)}\right)$, we obtain

the normal equations (Wapenaar *et al.* 2011b; van der Neut *et al.* 2011),

$$\hat{C}\left(\boldsymbol{x}_{\mathrm{R}}, \boldsymbol{x}\right) = 2\hat{A} \int_{\mathbb{S}_{\mathrm{rec}}} \hat{\tilde{G}}_{\mathrm{d}}^{(\mathrm{a})}\left(\boldsymbol{x}_{\mathrm{R}}, \boldsymbol{x}'\right) \hat{\Gamma}\left(\boldsymbol{x}', \boldsymbol{x}\right) \mathrm{d}\boldsymbol{x}', \tag{6}$$

where $\hat{C}\left(\boldsymbol{x}_{\mathrm{R}}, \boldsymbol{x}\right)$ is defined in eq. (2) and

$$\hat{\Gamma}\left(\boldsymbol{x}', \boldsymbol{x}\right) \equiv \sum_{j} \hat{v}\left(\boldsymbol{x}', \boldsymbol{x}_{\mathrm{S}}^{(j)}\right) \hat{v}^{*}\left(\boldsymbol{x}, \boldsymbol{x}_{\mathrm{S}}^{(j)}\right). \tag{7}$$

We refer to $\hat{\Gamma}\left(\boldsymbol{x}', \boldsymbol{x}\right)$ as the PSF. Eq. (6) states that the CCF is proportional to the sought-for dipole Green's function convolved with this PSF, where the latter quantifies the smearing of the virtual source in space and time. SI by MDD involves deconvolution of the CCF by the PSF in order to retrieve $\hat{\tilde{G}}_{\mathrm{d}}^{(\mathrm{a})}\left(\boldsymbol{x}_{\mathrm{R}}, \boldsymbol{x}'\right)$ (Wapenaar & van der Neut 2010). In practice, this deconvolution is often carried out in the frequency domain by solving the matrix equation associated with eq. (6). This requires discretization of the integral along $\mathbb{S}_{\mathrm{rec}}$ and hence assumes a regular sampling of the receiver coordinate $\boldsymbol{x}'$ (Wapenaar *et al.* 2011b). For details regarding the matrix inversion, we refer to van der Neut (2012). SI by MDD has been applied successfully to reflection data in an arctic environment (Poletto & Bellezza 2012), crosswell seismic reflection data (Minato *et al.* 2011) and ambient seismic surface-wave data (van Dalen *et al.* 2015; Weemstra *et al.* 2017a).

A few remarks regarding the difference between eq. (4), that is, SI by CC, and eq. (6), that is, SI by MDD, are in order. If the sources outside the region of interest (i.e. outside the region containing $\boldsymbol{x}_{\mathrm{R}}$) illuminate $\mathbb{S}_{\mathrm{rec}}$ uniformly and the medium is lossless, eq. (4) holds. This implies that any of the receivers at $\boldsymbol{x}$ along $\mathbb{S}_{\mathrm{rec}}$ can be turned into a perfect band-limited virtual source through computation of $\hat{C}\left(\boldsymbol{x}_{\mathrm{R}}, \boldsymbol{x}\right)$ according to eq. (2). In that specific case, the PSF of the SI by MDD formalism approaches a temporally and spatially band-limited delta function. In other words, the distortion of $C\left(\boldsymbol{x}_{\mathrm{R}}, \boldsymbol{x}, t\right)$ with respect to $\bar{G}_{\mathrm{d}}^{(\mathrm{a})}\left(\boldsymbol{x}_{\mathrm{R}}, \boldsymbol{x}', t\right)$ is limited to the convolution with $S(t)$ and a (frequency-dependent) scaling by $2\hat{A}$. In case the medium is not lossless and the one-sided illumination pattern not uniform, however, the deviation of $\hat{\Gamma}\left(\boldsymbol{x}', \boldsymbol{x}\right)$ from a spatial delta function can be significant. As such, the PSF blurs the source of the dipole Green's function in spatial directions. As mentioned before, this may limit monitoring capabilities and result in erroneous estimates of phase velocity. Through deconvolution by the PSF, SI by MDD, therefore, allows more accurate seismic monitoring and the extraction of more accurate phase velocities (e.g. Weemstra *et al.* 2017a).

2.3 Virtual-reflector seismology

The theory underlying SI by MDD originates from a so-called integral representation. Specifically, the Green's function between a source outside the medium of interest and a receiver inside that medium is represented by an integral over the boundary of that medium (Wapenaar & van der Neut 2010). The integrand of this integral is a sum of two terms, both involving a temporal convolution of the Green's function between the source and the boundary with the Green's function between the boundary and the receiver (Wapenaar *et al.* 2011b). Importantly, however, the Green's functions describing the wave propagation between the boundary and the receiver can be defined in a different medium than the Green's functions that describe the waves propagating from the source to the boundary. The latter Green's functions are associated with the actual medium, and hence with the Green's function between the physical source and the receiver, whereas the former Green's functions are defined between a virtual source and a receiver in a reference medium. As explained above, the theory underlying SI by MDD is derived by assuming the boundary of this reference medium to be of an absorbing nature.

Recently, Weemstra *et al.* (2017b) introduced an alternative simplification of the acoustic convolution-type Green's function representation by assuming reflecting boundary conditions along $\mathbb{S}_{\mathrm{rec}}$ in the reference medium. Considering the application to single-mode surface waves, we refer to the technique resulting from this simplification as VRS. In essence, VRS can be considered just another form of SI by MDD: both techniques involve a multidimensional deconvolution procedure. And because VRS can be derived from a simplification of the same convolution-type Green's function representation, its successful application also does not require the medium to be lossless. However, because $\mathbb{S}_{\mathrm{rec}}$, instead of being an absorbing boundary, is subject to reflecting boundary conditions in the reference medium, virtual-source responses retrieved through the application of VRS contain so-called virtual reflections from the receiver contour (Weemstra *et al.* 2017b). In this work, we investigate the suitability of these virtual reflections for the purpose of monitoring a non-scattering medium such as glacier ice.

Consider the configuration in the Fig. 1(c) (top). The region of interest, which does not contain any sources, is now enclosed by receivers. And, instead of being illuminated from one side only (which is the case for the configuration associated with SI by MDD), the receiver at $\boldsymbol{x}_{\mathrm{R}}$ is illuminated by single-mode surface waves from all directions. Contrary to the formulation underlying response retrieval through SI by CC, however, this illumination can be non-uniform. The variation in density and size of the depicted sources illustrates the non-uniform omnidirectional illumination. Again, the location of source number j is given by $\boldsymbol{x}_{\mathrm{S}}^{(j)}$. Assuming the contour $\mathbb{S}_{\mathrm{rec}}$ to be sufficiently smooth, the results obtained by Weemstra *et al.* (2017b) for acoustic media imply that for each of the sources,

$$\hat{v}\left(\boldsymbol{x}_{\mathrm{R}}, \boldsymbol{x}_{\mathrm{S}}^{(j)}\right) = \hat{A} \oint_{\mathbb{S}_{\mathrm{rec}}} \hat{\tilde{G}}_{\mathrm{d}}^{(\mathrm{r})}\left(\boldsymbol{x}_{\mathrm{R}}, \boldsymbol{x}'\right) \hat{v}\left(\boldsymbol{x}', \boldsymbol{x}_{\mathrm{S}}^{(j)}\right) \mathrm{d}\boldsymbol{x}'. \tag{8}$$

In this case, the dipole Green's function $\hat{\tilde{G}}_{\mathrm{d}}^{(\mathrm{r})}$ is defined as $\hat{\tilde{G}}_{\mathrm{d}}^{(\mathrm{r})}\left(\boldsymbol{x}_{\mathrm{R}}, \boldsymbol{x}'\right) \equiv [i\hat{c}/\omega] \nabla \hat{\tilde{G}}^{(\mathrm{r})}\left(\boldsymbol{x}_{\mathrm{R}}, \boldsymbol{x}'\right) \cdot \boldsymbol{n}$, and the integral is evaluated along a closed contour $\mathbb{S}_{\mathrm{rec}}$. Again, the bar indicates that $\hat{\tilde{G}}_{\mathrm{d}}^{(\mathrm{r})}$ is associated with a reference medium, which only inside $\mathbb{S}_{\mathrm{rec}}$ coincides with the actual medium. The superscript (r) indicates that now reflecting boundary conditions are assumed along $\mathbb{S}_{\mathrm{rec}}$ in this reference medium. Just as for $\hat{\tilde{G}}_{\mathrm{d}}^{(\mathrm{a})}$, the 2-D spatial derivative of $\hat{\tilde{G}}^{(\mathrm{r})}\left(\boldsymbol{x}_{\mathrm{R}}, \boldsymbol{x}'\right)$ is computed at $\boldsymbol{x}'$ along $\mathbb{S}_{\mathrm{rec}}$, and $\boldsymbol{n} = (n_1, n_2)$ is the outward pointing normal vector.

Apart from the factor two in front of the integral and the difference in $\mathbb{S}_{\mathrm{rec}}$ (open versus closed) eq. (8) is identical to eq. (5). Bear in mind, however, that the different boundary conditions imply that $\hat{\tilde{G}}_{\mathrm{d}}^{(\mathrm{r})}$ and $\hat{\tilde{G}}_{\mathrm{d}}^{(\mathrm{a})}$ are associated with different reference media. Physically, the absence of the factor two in eq. (8) can be explained by the reflecting nature of $\mathbb{S}_{\mathrm{rec}}$: the arrivals in $\hat{\tilde{G}}_{\mathrm{d}}^{(\mathrm{r})}$ that are not associated with reflections from $\mathbb{S}_{\mathrm{rec}}$ have simply twice the amplitude of the same arrivals in $\hat{\tilde{G}}_{\mathrm{d}}^{(\mathrm{a})}$. In fact, for the configuration in Fig. 1 [where $\mathbb{S}_{\mathrm{rec}}$ in (c) describes a closed contour that includes the open contour described by $\mathbb{S}_{\mathrm{rec}}$ in (b)], we have for all $\boldsymbol{x}'$ along $\mathbb{S}_{\mathrm{rec}}$ in eq. (5) that,

$$\hat{\tilde{G}}_{\mathrm{d}}^{(\mathrm{r})}\left(\boldsymbol{x}_{\mathrm{R}}, \boldsymbol{x}'\right) = 2\hat{\tilde{G}}_{\mathrm{d}}^{(\mathrm{a})}\left(\boldsymbol{x}_{\mathrm{R}}, \boldsymbol{x}'\right) + \text{‘virtual coda’}. \tag{9}$$

Here, the term 'virtual coda' captures all arrivals in $\hat{\tilde{G}}_{\rm d}^{(\rm r)}(\boldsymbol{x}_{\rm R},\boldsymbol{x}')$ that have reflected once or multiple times from the contour enclosing the region of interest.

Since eq. (8) holds for each $\boldsymbol{x}_{\rm S}^{(j)}$ individually, illumination by a multitude of sources effectively yields a set of equations. This set of equations can be solved in a least-squares sense for $\hat{\tilde{G}}_{\rm d}^{(\rm r)}$ (including $\hat{A}$). The normal equations describing this least-squares problem are obtained in the same way as they were obtained for SI by MDD: an auxiliary variable $\boldsymbol{x}$ along $\mathbb{S}_{\rm rec}$ is introduced [see Fig. 1(c), bottom] and both sides of eq. (8) are multiplied with $\hat{v}^*\left(\boldsymbol{x},\boldsymbol{x}_{\rm S}^{(j)}\right)$, giving,

$$\hat{C}(\boldsymbol{x}_{\rm R},\boldsymbol{x}) = \hat{A}\oint_{\mathbb{S}_{\rm rec}}\hat{\tilde{G}}_{\rm d}^{(\rm r)}(\boldsymbol{x}_{\rm R},\boldsymbol{x}')\,\hat{\Gamma}(\boldsymbol{x}',\boldsymbol{x})\,{\rm d}\boldsymbol{x}'. \tag{10}$$

The CCF and PSF are defined in eqs (2) and (7), respectively. The summation is now over all sources illuminating the region of interest, and not only the sources illuminating this region from one side [as is the case for the CCF and PSF associated with eq. (6)]. Contrary to SI by MDD, the reflecting boundary conditions imply that, even in case of a uniform omnidirectional illumination of the medium of interest, the PSF does not approach a temporally and spatially band-limited delta function.

Similar to SI by MDD, VRS involves deconvolution of the CCF by the PSF. In the case of eq. (10), however, this multidimensional deconvolution results in the retrieval of $\hat{\tilde{G}}_{\rm d}^{(\rm r)}(\boldsymbol{x}_{\rm R},\boldsymbol{x}')$. Although inversion of eq. (10) for $\hat{\tilde{G}}_{\rm d}^{(\rm r)}(\boldsymbol{x}_{\rm R},\boldsymbol{x}')$ is similar to inversion of eq. (6) for $\hat{\tilde{G}}_{\rm d}^{(\rm a)}(\boldsymbol{x}_{\rm R},\boldsymbol{x}')$, successful retrieval of $\hat{\tilde{G}}_{\rm d}^{(\rm r)}(\boldsymbol{x}_{\rm R},\boldsymbol{x}')$ relies on waves propagating inwards through $\mathbb{S}_{\rm rec}$ along its entire length and with all angles. Weemstra *et al.* (2017b) demonstrate this explicitly by synthesizing the PSF for a simple 1-D configuration. Importantly and contrary to SI by CC, however, variations in the amplitude of the inward propagating signal as a function of $\boldsymbol{x}'$ do not prevent successful response retrieval.

2.4 Extracting phase velocity

In Section 6, we compare phase-velocity dispersion curves extracted from responses obtained through SI by CC with dispersion curves extracted from the responses retrieved through SI by MDD. Additionally, these dispersion curves are compared against phase-velocity dispersion curves estimated using matched-field processing (e.g. Baggeroer *et al.* 1993). In this section, we therefore describe the theory and procedure associated with the extraction of phase-velocity dispersion from the interferometric responses. Matched-field processing is described in the next section.

Eq. (3) states that, in case of a uniform illumination of the receivers at $\boldsymbol{x}$ and $\boldsymbol{x}_{\rm R}$, the response retrieved through the application of SI by CC, that is, the CCF, is proportional to the Green's function between these two locations plus its complex conjugate, multiplied by $1/\hat{A}$ and $\hat{S}$. Using eq. (1) and the fact that $\hat{A}$, $\hat{S}$, ω and $\hat{c}$ are all real-valued, we can thus equate the zeros of the real part of $\hat{C}(\boldsymbol{x}_{\rm R},\boldsymbol{x})$ to the real part of $H_0^{(2)}\left(\hat{k}\,|\boldsymbol{x}_{\rm R}-\boldsymbol{x}|\right) + H_0^{(2)*}\left(\hat{k}\,|\boldsymbol{x}_{\rm R}-\boldsymbol{x}|\right)$. By considering the zeros, only, we discard amplitude information. Because $H_0^{(2)}\left(\hat{k}\,|\boldsymbol{x}_{\rm R}-\boldsymbol{x}|\right) \equiv J_0\left(\hat{k}\,|\boldsymbol{x}_{\rm R}-\boldsymbol{x}|\right) - iY_0\left(\hat{k}\,|\boldsymbol{x}_{\rm R}-\boldsymbol{x}|\right)$, where J_0 and Y_0 are zeroth-order Bessel functions of the first and second kind, respectively, we find that $H_0^{(2)}\left(\hat{k}\,|\boldsymbol{x}_{\rm R}-\boldsymbol{x}|\right) + H_0^{(2)*}\left(\hat{k}\,|\boldsymbol{x}_{\rm R}-\boldsymbol{x}|\right) = 2J_0\left(\hat{k}\,|\boldsymbol{x}_{\rm R}-\boldsymbol{x}|\right)$. Coincidence of the zeros implies that frequency values ω_j ($j=1,2,...$) can be identified for which both $\Re\left[\hat{C}(\boldsymbol{x}_{\rm R},\boldsymbol{x})\right]$ (the operator $\Re[...]$ maps its complex argument into its real part) and $J_0\left(\hat{k}\,|\boldsymbol{x}_{\rm R}-\boldsymbol{x}|\right)$ equate to zero. Assuming, for the moment, a lossless medium, we have that $\hat{k}=\omega/\hat{c}$. In that case, a set of phase velocities $\hat{c}_n(\omega_j)$ ($n=1,2,...$) exists, for each ω_j, for which $J_0\left(\omega_j\,|\boldsymbol{x}_{\rm R}-\boldsymbol{x}|/\hat{c}_n(\omega_j)\right)=0$. Selecting a single phase velocity $\hat{c}_n$ per ω_j, an array of phase velocities representing a single dispersion curve is obtained. Of all the different possible combinations of phase velocities, the one that gives the seismologically most plausible dispersion curve is chosen. By now, a large number of studies have used this technique to estimate phase velocity (e.g. Ekström *et al.* 2009; Tsai & Moschetti 2010; Boschi *et al.* 2013; Weemstra *et al.* 2017a).

The fact that the imaginary part of $H_0^{(2)}\left(\hat{k}\,|\boldsymbol{x}_{\rm R}-\boldsymbol{x}|\right) + H_0^{(2)*}\left(\hat{k}\,|\boldsymbol{x}_{\rm R}-\boldsymbol{x}|\right)$ equates to zero, implies that $\Im\left[\hat{C}(\boldsymbol{x}_{\rm R},\boldsymbol{x})\right]=0$ if all conditions associated with eq. (3) are fulfilled (the operator $\Im[...]$ maps its complex argument into its imaginary part). However, in case of a single-sided uniform illumination, instead of an omnidirectional uniform illumination, eq. (4) applies. In that case, the zeros of the real part of the CCF can still be equated to those of the zeroth order Bessel function of the first kind, but, additionally, the zeros of the imaginary part of the CCF, that is, the zeros of $\Im\left[\hat{C}(\boldsymbol{x}_{\rm R},\boldsymbol{x})\right]$, can be equated to the zeros of $-Y_0\left(\hat{k}\,|\boldsymbol{x}_{\rm R}-\boldsymbol{x}|\right)$. The procedure to obtain the candidate phase velocities $\hat{c}_n(\omega_j)$ ($n=1,2,...$) for each ω_j is similar to the one followed to obtain the candidate phase velocities using the zeros of the real part of the CCF. Note that the ω_j are different.

For the purpose of extracting phase-velocity dispersion from the virtual-source responses retrieved through SI by MDD, recall the definition of the dipole Green's function: $\hat{\tilde{G}}_{\rm d}^{(\rm a)}(\boldsymbol{x}_{\rm R},\boldsymbol{x}') \equiv [i\hat{c}/\omega]\,\nabla\hat{\tilde{G}}^{(\rm a)}(\boldsymbol{x}_{\rm R},\boldsymbol{x}')\cdot\boldsymbol{n}$. Furthermore, consider the fact that the Green's function describing a single-mode surface wave in the actual medium also describes single-mode surface wave propagation in the reference medium with absorbing boundary conditions. That is, eq. (1) also holds for $\hat{\tilde{G}}^{(\rm a)}$. By explicitly computing the spatial derivative of the zeroth order Hankel function and replacing the inner product with the normal to $\mathbb{S}_{\rm rec}$ by a minus sign, we find that $\hat{\tilde{G}}_{\rm d}^{(\rm a)}(\boldsymbol{x}_{\rm R},\boldsymbol{x}') \propto -iH_1^{(2)}\left(\hat{k}\,|\boldsymbol{x}_{\rm R}-\boldsymbol{x}'|\right)$. Using that $H_1^{(2)}\left(\hat{k}\,|\boldsymbol{x}_{\rm R}-\boldsymbol{x}'|\right) \equiv J_1\left(\hat{k}\,|\boldsymbol{x}_{\rm R}-\boldsymbol{x}'|\right) - iY_1\left(\hat{k}\,|\boldsymbol{x}_{\rm R}-\boldsymbol{x}'|\right)$, where J_1 and Y_1 are first-order Bessel functions of the first and second kind, respectively, we find that the zeros of the real part of the response retrieved through SI by MDD have to match the zeros of $-Y_1\left(\hat{k}\,|\boldsymbol{x}_{\rm R}-\boldsymbol{x}'|\right)$ and the zeros of the imaginary part of this response have to match the zeros of $-J_1\left(\hat{k}\,|\boldsymbol{x}_{\rm R}-\boldsymbol{x}'|\right)$. It is useful to note that, asymptotically, that is, for $|\boldsymbol{x}_{\rm R}-\boldsymbol{x}'| \gg 1/\hat{k}$, $-iH_1^{(2)}\left(\hat{k}\,|\boldsymbol{x}_{\rm R}-\boldsymbol{x}'|\right) = H_0^{(2)}\left(\hat{k}\,|\boldsymbol{x}_{\rm R}-\boldsymbol{x}'|\right)$. This implies that, at large separation between $\boldsymbol{x}_{\rm R}$ and $\boldsymbol{x}'$, relative to the wavelength, the phase of the response retrieved through SI by MDD can be expected to coincide with that of the response retrieved through the application of SI by CC. Provided, of course, the conditions associated with eq. (4) are fulfilled. Otherwise, the phase difference can be interpreted as a correction of the CCF resulting from the deconvolution by the PSF (e.g. Weemstra *et al.* 2017a).

A caveat should be made regarding the measurement of phase velocity between receivers whose separation is small with respect to the wavelength. From a theoretical point of view, the summation in eq. (2) can be replaced by a contour integral along the $\boldsymbol{x}_{\rm S}^{(j)}$. Halliday & Curtis (2008) evaluate this integral employing a stationary-phase

approximation, which essentially implies that an infinite-frequency assumption is made (Bender & Orszag 2013). Tsai (2009), instead, evaluates the integral explicitly. This author shows that the zeros of the imaginary part of the CCF should be equated to the zeros of $-\boldsymbol{H}_0\left(\hat{k}\,|\boldsymbol{x}_\mathrm{R}-\boldsymbol{x}|\right)$, instead to the zeros of $-Y_0\left(\hat{k}\,|\boldsymbol{x}_\mathrm{R}-\boldsymbol{x}|\right)$. Here, $\boldsymbol{H}_0$ is a Struve function of order zero. Even for a uniformly illuminated 2-D medium, therefore, the coincidence between the CCF and the Green's function deteriorates at distances small with respect to the wavelength. At distances larger than a few wavelengths, however, $\boldsymbol{H}_0(kr)$ and $Y_0(kr)$ behave very similarly (at a distance of three wavelengths, the maximum travel-time error has already reduced to 1.8 per cent; Tsai 2009). CCFs computed between receivers separated by less than a few wavelengths are, therefore, generally discarded in practical SI by CC applications (e.g. Yao *et al.* 2006). Note that the stationary-phase approximation and the explicit evaluation of the integral both result in a real part of the CCF that is proportional to a zeroth order Bessel function of the first kind. The zeros of the real part of the CCF between $\boldsymbol{x}_\mathrm{R}$ and $\boldsymbol{x}$ on the one hand, and zeros of $J_0\left(\hat{k}\,|\boldsymbol{x}_\mathrm{R}-\boldsymbol{x}|\right)$ on the other hand, therefore still coincide at short distances (Tsai 2009).

We finally note that in the case of a dissipative medium, $\hat{k}$ is complex-valued with its real and imaginary part coinciding with $\omega/\hat{c}(\omega)$ and α, respectively, that is, $\hat{k}=\omega/\hat{c}-i\alpha$, where α denotes the attenuation coefficient. For values of α that are small in the sense that $\alpha \ll \omega/\hat{c}$, the complex wavenumber can be approximated by $(\omega\,|\boldsymbol{x}_\mathrm{R}-\boldsymbol{x}|\,/\hat{c})\sqrt{1-(2i\alpha\hat{c}/\omega)}$ (Weemstra *et al.* 2015a). The Hankel function may in that case be approximated by $H_0^{(2)}\left(\omega\,|\boldsymbol{x}_\mathrm{R}-\boldsymbol{x}|\,/\hat{c}\,(\omega)\right)e^{-\alpha|\boldsymbol{x}_\mathrm{R}-\boldsymbol{x}|}$ (Tsai 2011). The procedure for estimating the phase velocity described above, therefore, applies equally well to dissipative media.

2.5 Matched-field processing

In the previous section, we have explained how to extract phase-velocity dispersion curves from interferometric medium responses. In order to test these dispersion curves for plausibility, we compare them to phase-velocity dispersion curves retrieved through the application of matched-field processing. In the following, we briefly outline the array processing technique matched-field processing as described by, for example, Corciulo *et al.* (2012), slightly adapted to our data set. Matched-field processing matches a synthetic wavefield calculated at the receiver locations for a point source at an arbitrary location and an arbitrary velocity model to those observed by the actual receivers. Accordingly, the best match is obtained if the actual source location and an appropriate velocity model are used for modelling the synthetic field. Allowing near-field point sources, hence circular wave fronts, matched-field processing is the generalization of the conventional plane-wave approach.

Consider the wavefield due to a source located at a surface point $\boldsymbol{x}_S$ recorded by a set of N receivers, also located at that surface. From the frequency domain, vertical particle velocity recorded by these receivers,

$$\hat{\boldsymbol{v}} \equiv \begin{pmatrix} \hat{v}_1\left(\boldsymbol{x}_{\mathrm{R},1},\boldsymbol{x}_\mathrm{S}\right) \\ \hat{v}_2\left(\boldsymbol{x}_{\mathrm{R},2},\boldsymbol{x}_\mathrm{S}\right) \\ \vdots \\ \hat{v}_N\left(\boldsymbol{x}_{\mathrm{R,N}},\boldsymbol{x}_\mathrm{S}\right) \end{pmatrix}, \tag{11}$$

the cross-spectral density matrix is calculated as

$$\hat{\boldsymbol{K}} = \hat{\boldsymbol{v}}\,\hat{\boldsymbol{v}}^\dagger, \tag{12}$$

where $\dagger$ denotes the conjugate transpose operation. To match the phase of the observed data, a synthetic replica vector for the source-receiver geometry under consideration is calculated. Matching only the phase and neglecting the amplitude information, it is given by

$$\hat{\tilde{\boldsymbol{v}}} = \begin{pmatrix} \hat{\tilde{v}}_1(a_1,\hat{c}) \\ \hat{\tilde{v}}_2(a_2,\hat{c}) \\ \vdots \\ \hat{\tilde{v}}_N(a_N,\hat{c}) \end{pmatrix}, \tag{13}$$

with

$$\hat{\tilde{v}}_l(a_l,\hat{c}) \equiv \exp\left(-i\left(\frac{\omega}{\hat{c}}a_l-\frac{\pi}{4}\right)\right), \qquad l=1,\ldots,N. \tag{14}$$

Again, surface waves travelling in a laterally homogeneous medium are assumed; hence a_l is the horizontal distance from the replica source location to the location of receiver l and $\hat{c}$ is the (frequency dependent) model velocity. Note that the exponent is equivalent to the exponent of the far-field approximation of the Hankel function in eq. (1). Finally, the phase matching is achieved by maximizing the output of the linear Bartlett processor

$$B = \sum_\omega \left|\hat{\tilde{\boldsymbol{v}}}^\dagger\,\hat{\boldsymbol{K}}\,\hat{\tilde{\boldsymbol{v}}}\right|. \tag{15}$$

This may be achieved by averaging over a set of discrete frequencies from a certain band of interest where the surface wave velocity is assumed constant (or only slightly varying). Typically, a 2-D grid search over the source location and the model velocity is performed. However, in case the source location is known, as is the case for our active-source data, we only need to find the model velocity matching the observations best.

3 DATA AND PROCESSING

For this study, we use both synthetic and active source seismic data. The synthetic data is modelled using the same geometry as the one associated with the active data. This geometry is shown in Fig. 2: Two parallel receiver lines (each consisting of 16 receivers) and a single receiver between these receiver lines are illuminated by 76 sources on either side of the 'receiver cavity'. Receivers and sources are regularly spaced along the lines, resulting in separations of 5 and 1 m, respectively.

The active-source data was acquired on Glacier de la Plaine Morte located in the Bernese Alps, Switzerland. Glacier de la Plaine Morte is the largest plateau glacier in the European Alps (Huss *et al.* 2013) and of special interest because of the sudden (and potentially hazardous) annual drainage event of an ice-marginal lake. Its maximum ice thickness is roughly 200 m and in the deployment area (Fig. 2), it is around 50 to 100 m (Huss *et al.* 2013). The receiver lines consisted of Geospace GS-11D geophones with a corner frequency of 4.5 Hz and were digitized with a Geometrics Geode at a sampling frequency of 2000 Hz. The single receiver between the lines was a PE-6/B geophone with the same corner frequency but a slightly different instrument response. It was connected to an Omnirecs DataCube sampling at 400 Hz. All geophones were installed with spikes directly on the ice. To allow the penetration of the spikes, the ice was crushed and the geophones were covered with ice to avoid tilting due to melt. For signal excitation, a seismic sledgehammer hitting a metal plate on the glacier's surface was used. At each shot location (76 on either side of the receiver cavity), at least five shots were performed. All data were acquired on 2016 September 7 within 2 hr.

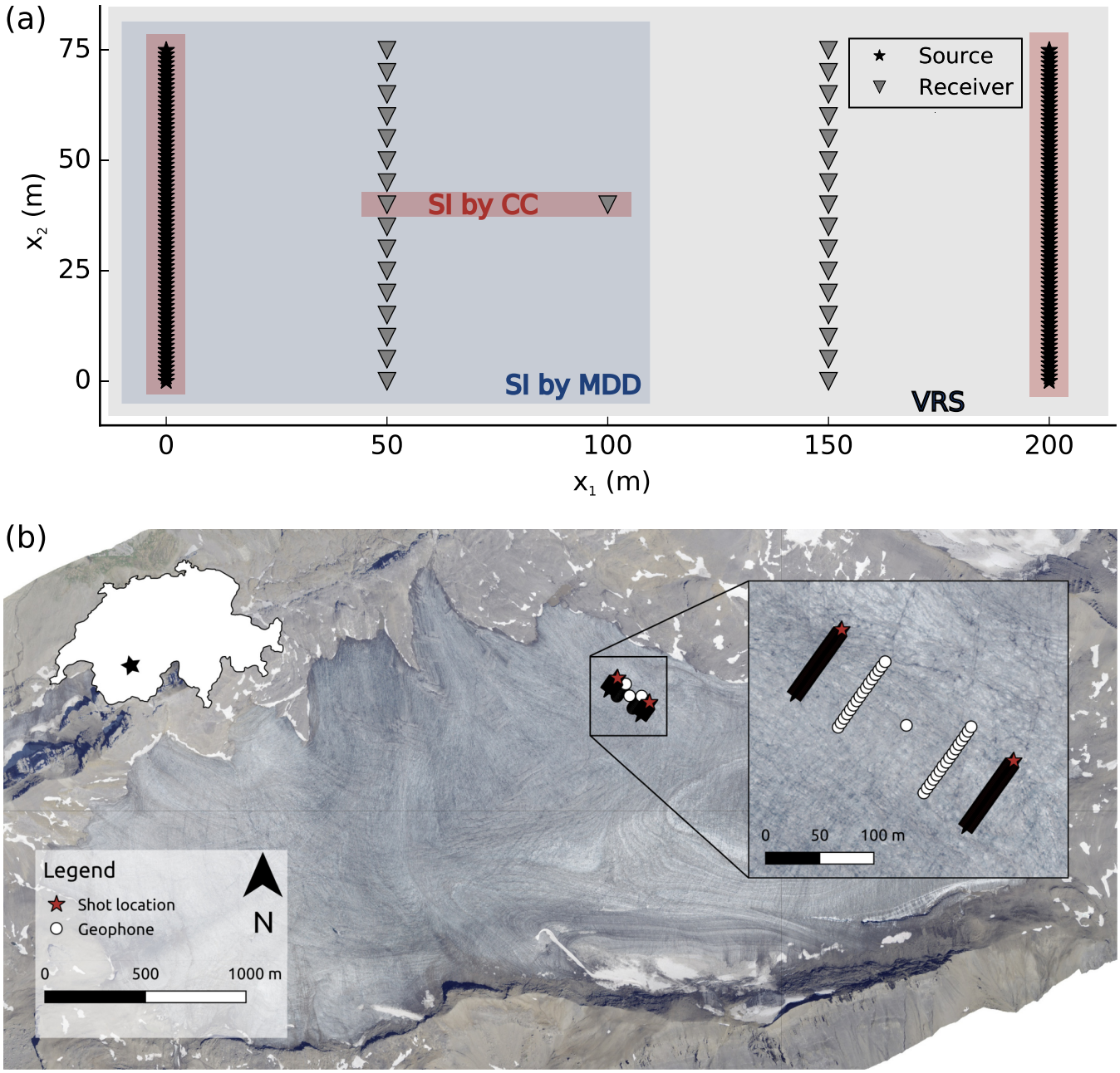

Figure 2. (a) Source–receiver geometry used for synthetic and field data. Two receiver lines (each consisting of 16 sensors) are placed equidistant to a centre receiver. 76 evenly spaced sources on both sides illuminate the receiver cavity. The background colours indicate which parts of the setup are used for SI by CC (red), SI by MDD (blue) and VRS (grey). Note that for the computation of the CCF, only the left source line is used in some instances (when compared to SI by MDD). (b) Orthophoto of Glacier de la Plaine Morte in Switzerland's Canton Bern. The white inset in the upper left-hand corner shows the outline of Switzerland and the field site indicated by the black star. The second inset shows the source and receiver locations in the field.

Contrary to the data from the centre receiver, GPS synchronization was not available for the line receivers. For this reason, a single geophone (identical to the centre one) was placed adjacent to the first sensor of both receiver lines allowing synchronization of the latter to GPS time. In this process, we first corrected the data from all sensors for instrument response and decimated the receiver line recordings to 400 Hz sampling frequency. Then, we determined the time shift between the neighbouring geophones for each multishot data packet from a single-shot location. Since the distance between the receivers was a few decimetres, only, we expect the traveltime between these receivers to be negligible. This processing was done in the frequency domain and for the two receiver lines individually, using shots on the appropriate side to ensure a high signal-to-noise ratio. Data from all line receivers were shifted by the determined phase shift and transformed back to the time domain.

Fig. 3 exemplifies the vertical component particle velocity associated with a single active shot. The recorded seismogram is typically characterized by weak body waves and a dominant (single-mode) Rayleigh wave. Apart from having a higher frequency content, the active shots strongly resemble naturally occurring shallow icequakes associated with crevasse opening (e.g. Walter *et al.* 2009). Events of this type exhibit a frequency range of roughly 10 to 50 Hz

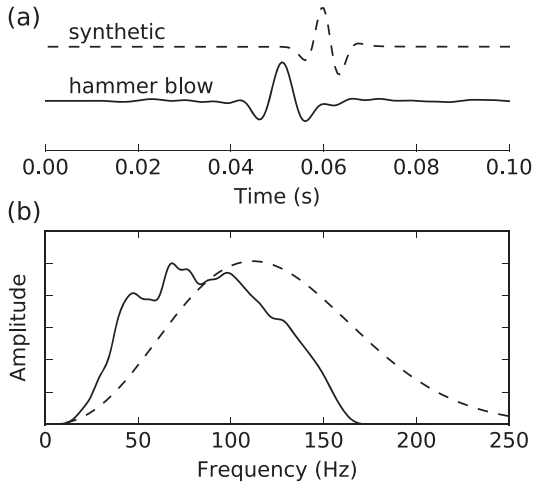

Figure 3. (a) Synthetic signal and typical hammer blow signal. The glacier data are upsampled from 400 to 2000 Hz for illustration purposes. (b) Corresponding amplitude spectra of the two signals.

and make up the vast majority of glacial seismicity (Podolskiy & Walter 2016).

The targeted glacier signals appear to be dominated by a single-mode surface wave. Such waves behave very similar to acoustic waves propagating through a homogeneous 2-D acoustic medium. We, therefore, model single-mode Rayleigh waves using the open source code for acoustic wave propagation described in Thorbecke & Draganov (2011). As a source-time function, we use a Ricker wavelet with a central frequency of 100 Hz. Fig. 3 shows a qualitative comparison between a synthetic signal and the response to a glacial hammer blow.

4 PROOF OF CONCEPT: SI BY MDD AND VRS

4.1 Synthetic data

The synthetic data used in this section were created for a homogeneous subsurface with a velocity of 1650 m s^{-1}. This is a typical velocity for Rayleigh waves exclusively sensitive to glacier ice (Walter *et al.* 2015). We first apply SI by MDD to this data, and compare the retrieved responses to the responses retrieved through the application of SI by CC. This implies that we consider a one-sided (potentially non-uniform) illumination. To that end, we let $\mathbb{S}_{\text{rec}}$ in eq. (5) coincide with the left receiver line, that is, the line of receivers along $x_1 = 50$ m. Because of the considered one-sided illumination, we do not consider sources along the right line of sources, that is, along the line $x_1 = 200$ m. The computation of the CCF (eq. 2) hence only involves a summation over the sources along the line $x_1 = 0$ m. The same applies for the computation of the PSF in eq. (7). All 76 sources along this line are excited. The configuration associated with SI by MDD is indicated in blue in Fig. 2 (a). The configuration associated with SI by CC is indicated in red in Fig. 2 (a) (although the sources along $x_1 = 200$ m are not included in this particular computation of the CCF).

SI by MDD involves solving eq. (6) for $\hat{\tilde{G}}_{\text{d}}^{(\text{a})}$, that is, we deconvolve the CCF by the PSF. Note that, implicitly, the factor $2\hat{A}$ is included in the retrieved dipole Green's function. Since the receivers along the contour are spaced regularly, the integral in eq. (6) can be

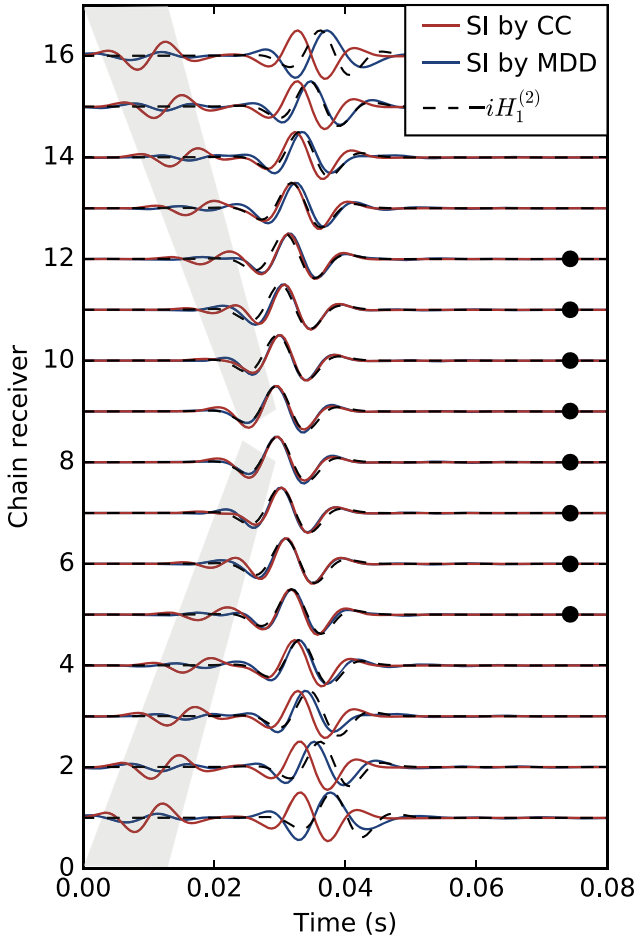

Figure 4. Virtual-source responses retrieved through the application of SI by CC and SI by MDD along with the modelled dipole Green's functions $-i\,H_1^{(2)}\left(\hat{k}\,|\boldsymbol{x}_{\text{R}} - \boldsymbol{x}'|\right)$ for all 16 virtual sources along the line $x_1 = 50$ m. These responses are retrieved at the centre receiver. Note that the latter two are convolved with the source's power spectrum. The grey shaded areas indicate the approximate times of the truncation arrivals. Black dots indicate waveforms associated with receiver pairs having sources in the stationary phase direction.

readily discretized such that solving for $\hat{\tilde{G}}_{\text{d}}^{(\text{a})}$ is achieved by calculating the dot product of the CCF matrix and the inverse of the PSF matrix. In practice, computation of the inverse involves Tikhonov regularization (Hunziker *et al.* 2009). The subsequent deconvolution is performed for each discrete frequency independently. Responses retrieved through the application of SI by CC are convolved with the autocorrelation of the source's spectrum (eq. 3), whereas responses retrieved through the application of SI by MDD are not. In order to make a fair comparison between the two different methodologies, we also convolve the SI by MDD responses with the power spectrum of the sources, which in our case is the autocorrelation of a ricker wavelet with a central frequency of 100 Hz. Fig. 4 compares the virtual-source responses retrieved through the application of SI by MDD to the virtual-source responses retrieved through the application of SI by CC (i.e. the CCFs). The 16 receivers along $x_1 = 50$ m act as virtual sources, and their responses are retrieved at the centre receiver. We recall from Section 2.4 that the response retrieved through SI by MDD are proportional to $-i\,H_1^{(2)}\left(\hat{k}\,|\boldsymbol{x}_{\text{R}} - \boldsymbol{x}'|\right)$. Since

$|\boldsymbol{x}_R - \boldsymbol{x}'| \gg 1/\hat{k}$ holds for most frequencies considered, we expect the responses from SI by CC and SI by MDD to be in phase.

In Fig. 4, the corrections resulting from the application of SI by MDD manifest themselves in two features. First, SI by MDD corrects the phase distortions of the retrieved SI by CC responses, which are introduced by the non-uniform illumination. These distortions are especially severe for off-horizontal receiver pairs (line receivers closer to the margin) because of the resulting unfavourable source distribution (i.e. no sources in the stationary-phase direction). For instance, even though there are no sources in the stationary-phase direction when using chain receiver 1 (i.e. using the lowermost line receiver with coordinates $x_1 = 50$ m and $x_2 = 0$ m), SI by MDD still captures the phase of the true medium response, while the phase retrieved through SI by CC is severely biased. For receiver combinations having sources in the stationary phase direction (e.g. chain receiver 8), the phase of the response retrieved through SI by CC already is accurate, which is why SI by MDD does not alter it and both waveforms coincide. Second, a strong truncation arrival caused by the finite length of the source line (grey shaded area in Fig. 4) is discernible in the responses retrieved through the application of SI by CC. These spurious arrivals arise because contributions to the CCF from outside the stationary-phase directions do not interfere destructively when the source distribution is truncated at finite distance (e.g. Snieder *et al.* 2008). This is the case for our line of sources along $x_1 = 0$ m (see Fig. 2). SI by MDD effectively corrects for these artefacts and significantly decreases their amplitude. This is visible for receivers 1 to 6 and 11 to 16 since the truncation arrival is sufficiently separated in time from the actual response in these cases (i.e. arrives earlier than the actual response). For the virtual sources in between, the actual response and the truncation arrival interfere, which is why the latter is not directly discernible. We note that the truncation arrival may be suppressed by tapering the strength of the sources at the edges of the source line. However, we do not consider this processing step here, since it—even though it suppresses the truncation arrival—causes the retrieved actual phase of the SI by CC responses to deviate stronger from the theoretical waveform than without the source tapering. Again, this is especially severe for the receiver pairs without sources in the stationary-phase direction, since the source tapering is a further degradation in illumination pattern. This effect is particularly pronounced due to the relatively short source aperture of our setup.

Because of the one-sided illumination, only the responses at positive time are retrieved in this example. Let us now also consider a two-sided illumination by including the right side of the source-receiver configuration in Fig. 2 (i.e. we use all sources and all receivers), that is, we apply VRS. From eq. (10), it can be seen that the retrieval of VRS responses, $\hat{\tilde{G}}_d^{(r)}(\boldsymbol{x}_R, \boldsymbol{x}')$, is identical to the retrieval of SI by MDD responses. However, as explicitly stated in eq. (9), $\hat{\tilde{G}}_d^{(r)}(\boldsymbol{x}_R, \boldsymbol{x}')$ does not only contain the direct wave, but also virtual reflections from the receiver contours. Note that, similar to the dipole Green's function retrieved through the application of SI by MDD, the factor $\hat{A}$ is included in the retrieved response. Using the source-receiver setup depicted in Fig. 2 and the same processing steps as for SI by MDD, we indeed obtain a response containing virtual reflections. Fig. 5 presents the response associated with the virtual-source receiver pair surrounded by the horizontal red box in Fig. 2. All virtual-source responses in the remainder of this work are associated with this receiver pair. For comparison, we also show the SI by MDD result again. As expected, when using a two-sided illumination, application of SI by CC results in the retrieval of responses at positive and negative time. Application of VRS, in contrast, renders the peak at negative time almost zero and generates a series of reflections: the reflecting boundary condition along the receiver lines at $x_1 = 50$ m and $x_1 = 150$ m causes these lines to act as a physical boundary, which causes the response to bounce back and forth in the receiver cavity. Numerous reflections are obtained, each of them introduces a change in polarity and the amplitude slowly decays. This example demonstrates that, in principle, our source-receiver geometry is suitable for the application of VRS.

4.2 Glacier data

The synthetic data used in the previous section are free of noise and the associated medium is non-dissipative. Here, we apply the virtual-source methods to field data recorded on a glacier, hence, the data quality is lower and the medium dissipative. Before doing so, we visually inspect the data and discard all hammer blows that are either very noisy or not recorded properly by all receivers. Altogether, the selected data set consists of 360 hammer blows on either side and at least three shots are available from each shot location along the source lines. Since the shot data are dominated by single-mode Rayleigh waves, we calculate CCF and PSF as described by eqs (2) and (7), respectively. Furthermore, we again solve for $\hat{\tilde{G}}_d^{(r)}$ and $\hat{\tilde{G}}_d^{(a)}$ as described earlier. Note that the amount of regularization required for calculating the inverse of the PSF matrix might be different for SI by MDD and VRS in order to obtain reasonable results. First, we consider the case of 2×76 (for SI by MDD, we use again only 76 sources, i.e. only the source line at $x_1 = 0$ m) regularly spaced sources (solid lines in Fig. 6). Similar to the case of synthetic data, we successfully obtain the desired responses: A direct wave arrival for SI by CC and SI by MDD, and the direct wave arrival plus reverberations from the receiver contours for VRS. Even though the reflections are weaker in amplitude compared to the synthetic data, at least five are discernible (arrows in Fig. 6). Note that, for aesthetic reasons, also in this case the SI by MDD and VRS responses are convolved with the autocorrelation of a Ricker wavelet.

In Fig. 6, we also show the effect of a reduced shot number: We consider 25 randomly selected source locations from each source line (multiple shots per location possible). Using this source distribution (Fig. 6c) results in a severe phase distortion of the virtual-source response retrieved through the application of SI by CC. This is understandable since the sources are distributed unevenly. In contrast, responses retrieved through the application of SI by MDD and VRS barely differ from the scenario of regularly spaced sources. Both methods capture the unfavourable illumination pattern and remove its imprint from the CCF through the deconvolution process. This example again demonstrates the effectiveness of multidimensional deconvolution procedures in correcting for illumination-related artefacts. Additionally, since the source distribution depicted in Fig. 6(c) is relatively coarse and uneven, this result suggests that relatively stable responses can be obtained from small amount of field data by the application of SI by MDD and VRS. The latter includes a reflection coda that is also largely unaffected by the degradation of the illumination pattern.

5 MONITORING PERSPECTIVES

According to theory and as shown in the previous section, SI by MDD and VRS are effective in accounting for non-uniform medium

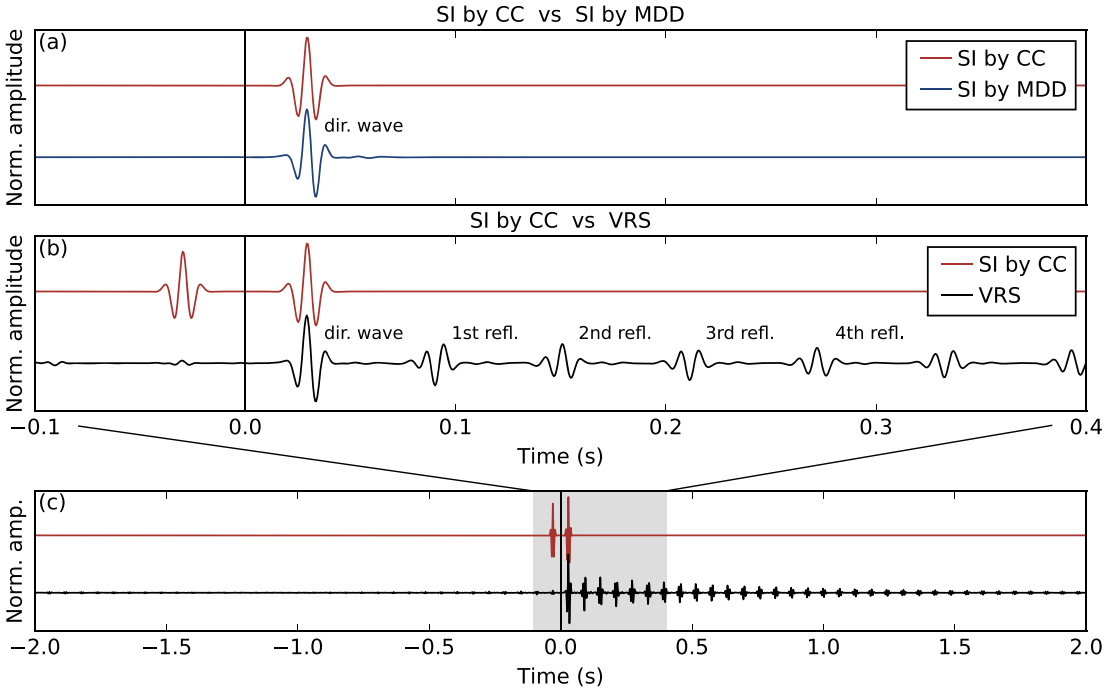

Figure 5. (a) Virtual-source responses retrieved through the application of SI by CC and SI by MDD for a one-sided illumination. (b) Virtual-source responses retrieved through the application of SI by CC and virtual-reflector seismology (VRS). (c) Full length records of (b). The grey shaded area indicates the window depicted in (b). Note that numerous virtual reflections arise when using VRS.

illumination. We expect this to be beneficial for monitoring applications since the retrieved responses are more stable in the case of uneven source distributions or moving/propagating sources, that is, if the source distribution is time-dependent. Additionally, the virtual reflections are expected to improve monitoring applications because they sample the medium more densely and additionally allow several measurements of coda traveltime shifts. In the following, we investigate the monitoring perspectives of SI by MDD and VRS.

5.1 Measurement of small velocity changes

For the measurement of small relative velocity changes $\mathrm{d}v/v$, two approaches are widely used. One of them is called moving-window cross-spectral (MWCS) analysis (Poupinet *et al.* 1984; Ratdomopurbo & Poupinet 1995). Its basic principle is to compare a record h, to a reference record from a different date, h_{ref}. A time window at a certain lapse time t is cut from each record. If the waveforms in both time-windows are similar enough, resulting in a high cross-coherence, the time shift δt is determined in the frequency domain. The time shift is proportional to the slope of the unwrapped phase in the cross-spectrum. By repeating this analysis for a series of time-windows in the coda, several estimates of δt are obtained. In the case of a homogeneous velocity change, the time delay experienced by the wavefield will increase linearly with lapse time. The velocity change finally is related to the average slope of a linear regression on the δt as a function of t, that is, $\mathrm{d}v/v = -\delta t/t$. For a detailed account of the MWCS method, the reader is referred to Clarke *et al.* (2011).

The second method, commonly referred to as the 'stretching' method, considers the whole coda portion of the signal at once. Typically, the used time window starts after the direct arrivals and locally scattered waves, and can span up to the point where the coda disappears into the noise level. Again assuming a homogeneous velocity change in the medium, the resulting δt is linearly dependent on t. In other words, the perturbed signal is stretched or compressed in a linear fashion along the time axis. The latter can be measured by interpolating the perturbed coda at times $t(1-\epsilon)$ with various candidate values for velocity variations ϵ. For each value, the correlation coefficient between the stretched signal h and the reference waveform h_{ref} is calculated:

$$CC(\epsilon) = \frac{\int_{t_1}^{t_2} h(t(1-\epsilon))h_{ref}(t)\mathrm{d}t}{\sqrt{\int_{t_1}^{t_2} h^2(t(1-\epsilon)\mathrm{d}t \int_{t_1}^{t_2} h_{ref}^2(t)\mathrm{d}t}}, \tag{16}$$

where t_1 and t_2 are the start and end time of the coda used, respectively. The actual relative velocity change $\mathrm{d}v/v$ corresponds to the value of ϵ that maximizes the correlation-coefficient between the waveforms. In the following, we refer to this method as stretching technique. For details and a comparison of the stretching method to MWCS, the reader is referred to Hadziioannou *et al.* (2009).

5.2 Application to numerically modelled data

Typically, both MWCS and stretching are applied to later arriving coda waves. In our case, however, responses retrieved through the application of SI by CC and SI by MDD consist predominantly of a single ballistic surface wave. Because these waveforms are of limited duration, the application of MWCS to several successive time windows is not possible. For this reason, we restrict our $\mathrm{d}v/v$ analysis of SI by CC and SI by MDD responses to the stretching technique, even though we do not expect a linear dependence of δt on t for the direct arrivals. In contrast, VRS yields the ballistic surface wave plus virtual surface-wave reflections from the receiver contour. Consequently, MWCS can readily be applied to the VRS responses. Additionally, since we only consider spatially homogeneous velocity variations, the time delay within windows containing

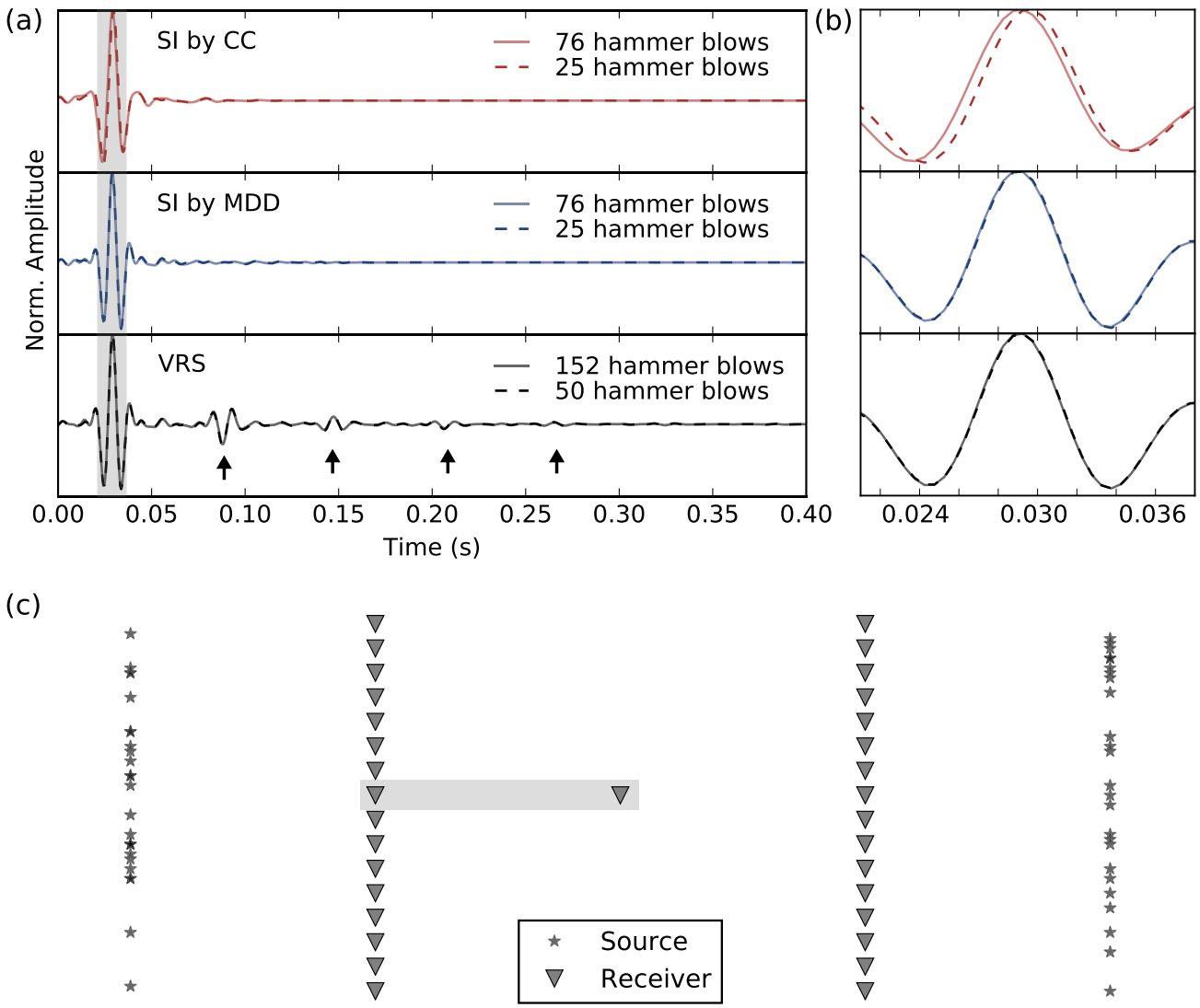

Figure 6. (a) SI by CC (red), SI by MDD (blue) and VRS (black) applied to glacier data. The methods were applied to data from (2 ×) 76 regularly spaced (solid lines) and (2 ×) 25 randomly spaced (dashed lines) hammer blows. The responses are obtained for the receiver pair surrounded with the grey shaded area in (c). The black arrows point at the virtual reflections retrieved through VRS. (b) Zoom into the grey shaded area of (a). (c) Random source distribution used for the 50 sources case.

the ballistic waves and reflections is constant with respect to the reference record h_{ref}. Thus, we use MWCS to measure relative velocity variations from reflection coda (even though we find that stretching yields similar results). For this purpose, we use the MWCS algorithm implemented in the MSNoise package (Lecocq *et al.* 2014).

Before we consider realistic monitoring scenarios, we test our framework and the measurement of small velocity changes as described above on two simple synthetic data sets. First, we apply SI by CC, SI by MDD and VRS to data from two homogeneous models with velocities of 1650 and 1641.75 m s^{-1} resulting in $dv/v = -8.25/1650 = -0.005$. SI by CC and SI by MDD responses are calculated from 76 regularly spaced sources (one source line) and VRS responses from 2 × 76 regularly spaced sources (two source lines) with unit amplitude (see Fig. 2). Fig. 7 shows the virtual-source responses for the three methods and the two medium velocities. We observe that the decrease in velocity is better observable from the (later-arriving) virtual reflections; the velocity change is barely discernible upon visual comparison of the ballistic surface waves. As discussed above, we apply stretching to a window of 0.06 s long windows centred around the direct arrival of the SI by CC and SI by MDD responses and MWCS to VRS responses in order to measure dv/v. For the latter, we restrict our analysis to five non-overlapping windows of 0.06 s centred around the direct arrival and the first four virtual reflections (windows indicated by black vertical lines in Fig. 7c). In doing so, we apply the same processing to the field data, where four reflections are discernible as well (see Fig. 6).

For the described case, SI by CC, SI by MDD and VRS yield a dv/v value of −0.0049. These values are reasonably close to the true value, suggesting that using the direct wave only results in robust measurements given the relatively homogeneous source distribution considered. Additionally, we test whether the reflections, indeed, are only sensitive to the medium between the receiver lines. For this purpose, we perturb the model velocity only outside the receiver cavity, that is, between the source and receiver line on either side of the cavity such that the medium in the receiver cavity is not altered. To prevent the changes in the illumination pattern caused by scattering

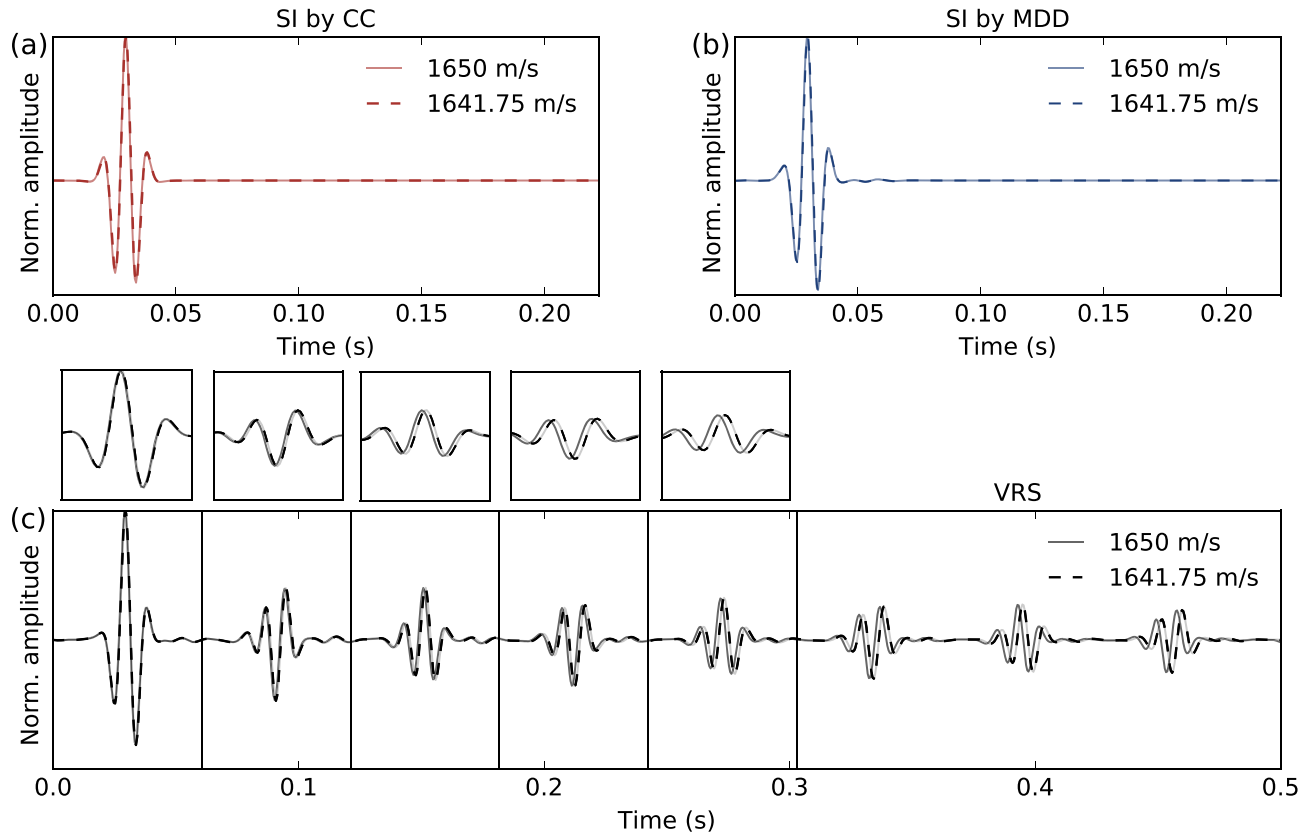

Figure 7. Virtual-source responses retrieved from synthetic acoustic data of two homogeneous velocity models (1650 and 1641.75 m s^{-1}). (a) SI by CC responses. (b) SI by MDD responses. (c) VRS responses. Recall that the depicted virtual-source responses are associated with the receiver pair surrounded by the red box in Fig. 2 (a). Black vertical lines delimit the windows used for dv/v measurements (for details see text). The insets are a zoom of the windows below. Note that the velocity variations can be detected visually from the later arriving reflections.

off the introduced heterogeneities, we taper the edges of these heterogeneities. Because surface waves traversing the heterogeneities will encounter smooth velocity transitions, changes in the illumination pattern due to scattering are unlikely. This can be confirmed by looking at the maximum correlation coefficient after stretching: if it is not different in the homogeneous case and the smoothed 'heterogeneous' case, the waveform was not affected strongly by the lateral change in medium properties. As expected, we do not find any velocity variation with respect to the homogeneous 1650 m s^{-1} medium, which confirms that the virtual reflections are, indeed, only sensitive to the area bound by the receiver contours.

Now, we consider a realistic scenario with time-dependent source distributions mimicking icequake clustering both in space and time as found, for example, by Mikesell *et al.* (2012). In other words, we model different source distributions to calculate the two responses which, in turn, are used to measure relative velocity changes. Again, we model acoustic waves in the homogeneous 1650 and 1641.75 m s^{-1} media for regularly spaced sources; however, before computing the responses, we multiply the seismograms of each source with a random integer from the range 1–2. To achieve statistical relevance, we repeat this analysis 500 times, that is, we obtain 500 independent dv/v realizations, each of them resulting from a random source distribution. Fig. 8 shows that the SI by CC is strongly affected by assuming time-varying sources and varying source strengths. Even though the resulting histogram is centred around the expected value, the single estimates scatter considerably and are off by a factor of three in some cases. In contrast, the same processing technique for dv/v measurements (stretching) applied to SI by MDD responses performs significantly better, causing maximal deviations from the true value of around 25 per cent. Additionally, more than half of the measurements cluster in the bin centred around the true value. Even less spread is achieved when virtual reflections are included in the dv/v measurement: almost all of the 500 dv/v values are contained in the bin centred around the true value.

Next, we consider greater irregularities in the source distribution by allowing the source amplitudes to vary between one and five (integer-wise). As expected, the histograms slightly broaden for all three methods, thereby indicating less accurate dv/v estimates. The degradation of the accuracy, however, is minor considering the increased level of non-uniformity of the illumination pattern.

5.3 Application to field data

For the field data, a similar analysis is performed. Recall that for each shot location, several shots (at least three) are available. Furthermore, the source strength is shot-dependent, because the signal-generating downward force caused by the rapid deceleration of the hammer is different for each hammer blow. Consequently, by randomly selecting a single hammer blow for each source location, a similar modulation of the sources' amplitudes is obtained. And, just as for the numerically simulated data, we compare the different interferometric methodologies for a total of 500 realizations. Since all hammer blows were performed within 2 hr, we do not expect any relative velocity variation.

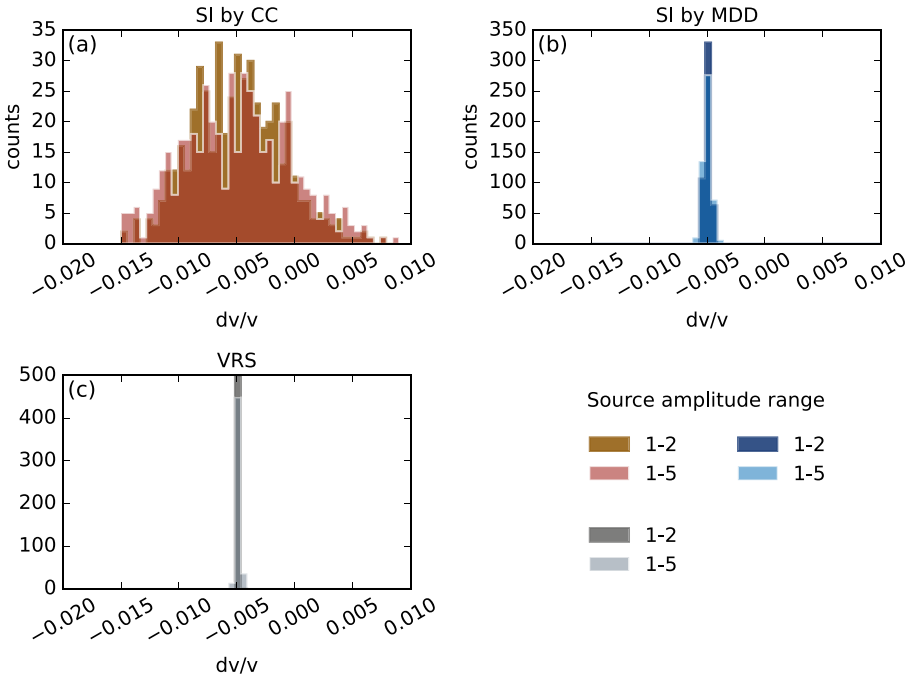

Figure 8. (a) SI by CC, (b) SI by MDD and (c) VRS applied to acoustic synthetic data: dv/v measurements obtained from virtual-source responses for two media with slightly different velocities (1650 versus 1641.75 m s^{-1}; dv/v= -0.005). The responses are calculated for the source distribution depicted in Fig.2 (regularly spaced sources). However, seismograms from each source are multiplied with a random integer from the range 1–2 and 1–5 (see legend) before calculating the responses. 500 dv/v measurements are shown, each is obtained by comparing responses calculated for the two media from two random source distributions sampling the 1650 and 1641.75 m s^{-1} media.

Similar to the case of synthetic data in the previous section, the accuracy of the dv/v measurements is highest for VRS, followed by SI by MDD and SI by CC (Fig. 9). The velocity variations retrieved through the application of VRS vary between −0.23 and 0.23 per cent, whereas they vary between −0.3 and 0.3 per cent and −0.6 and 0.6 per cent for SI by MDD and SI by CC, respectively. In case of SI by CC, some dv/v measurements yield unrealistic values of 0.5 per cent velocity variation or higher.

Next, we decrease the number of sources, that is, we calculate both the reference response h_{ref} and the current response h using only (2 ×) 25 randomly chosen sources. Furthermore, we allow multiple hammer blows from a single-shot location. This time, we also measure 500 dv/v values, each of them calculated from two random source distribution responses. By doing so, the differences in performance between the different methods become considerably larger. From Fig. 9, it can be seen that by decreasing the number of sources, SI by CC measurements are highly error-prone: numerous estimates incorrectly suggest velocity variations as large as 1 per cent or higher. Additionally, the dv/v distribution does not clearly peak at the zero velocity variation value, showing that SI by CC is not capable of accurately measuring velocity variations for the setup under consideration. Similarly, but less severe, SI by MDD precision is strongly degraded. Even though still peaking at zero per cent velocity variation, the large spread of the measurements does not allow an accurate determination of dv/v. In contrast, VRS still accurately determines vanishing dv/v, even though the dv/v histogram is slightly broadened. Nevertheless, more than 96 per cent of all measurements are contained in the velocity-variation range of −0.23 to 0.23 per cent, showing that dv/v is well constrained when using VRS.

5.4 Discussion

In this section we have demonstrated that, when it comes to the distribution of sources, the MDD techniques (i.e. SI by MDD and VRS) relax the conditions for seismic monitoring. In particular, these techniques reduce the amount of data needed to retrieve a stable virtual-source response and thus hold the promise to increase the temporal resolution of monitoring studies. This applies especially to VRS: the virtual reflections from the receiver contour result in artificial coda. As such, VRS effectively makes up for the lack of natural coda due to the relative homogeneity of ice bodies.

Unlike in the setup used in this study, a straight line of sources is typically not found in nature. However, as shown, for example, by Neave & Savage (1970), Roux *et al.* (2010), Mikesell *et al.* (2012) and Walter *et al.* (2015), shallow icequakes characterized by a dominant Rayleigh wave are numerous and generally spatially varying as a function of time. These shallow icequakes do not need to be distributed such that the generated Rayleigh waves illuminate the region of interest uniformly from all angles: provided their distribution ensures that no large angles are left without energy flux, application of VRS is possible. Moreover, VRS does allow the icequakes' magnitudes to vary, as the multidimensional deconvolution process corrects the retrieved cross-correlation responses for artefacts resulting from the associated amplitude variations. We finally note that the normal equation (eq. 10) is equally valid for a set of equidistant icequakes with varying amplitudes as for a set of icequakes at various distances. By (i) randomly modulating the strength of the line sources and (ii) selecting subsets of sources, we have therefore effectively modelled random spatial distributions of icequakes.

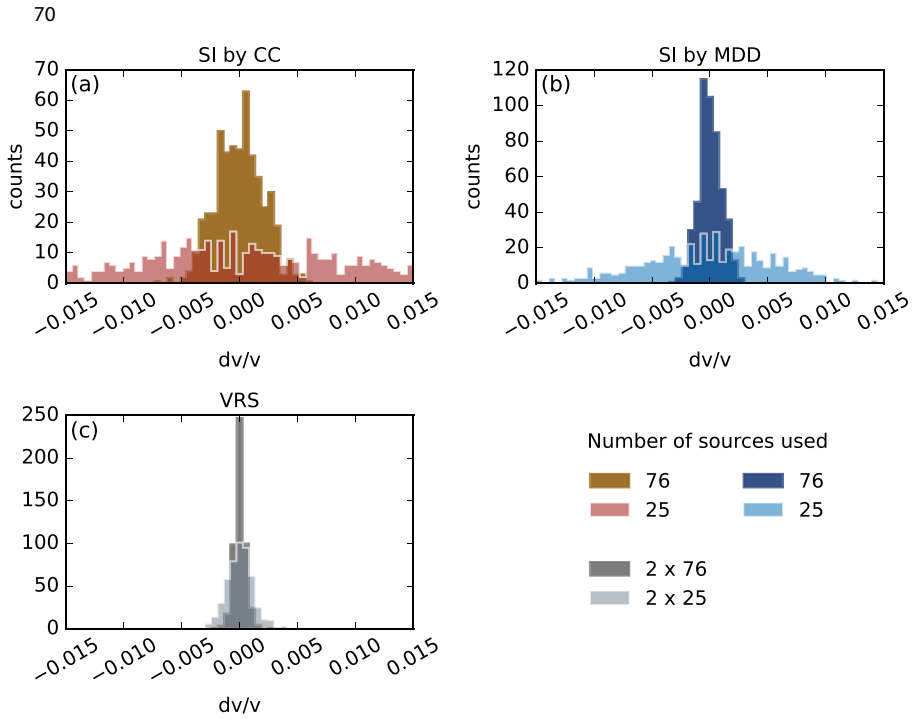

Figure 9. (a) SI by CC, (b) SI by MDD and (c) VRS applied to glacier data: dv/v measurements obtained by comparing responses resulting from different source distributions. Two cases are considered: 1. The responses are calculated for the source distribution depicted in Fig. 2[(2 ×) 76 regularly spaced sources], however, for each shot location a random shot is picked (multiple shots are available for each location). 2. (2 ×) 25 random shots are picked for response calculation (multiple shots for a single-shot location possible). 500 dv/v measurements are shown, each is obtained by comparing two randomly chosen source subsets.

6 EXTRACTING DISPERSION CURVES

Besides monitoring applications, the estimation of phase velocity dispersion from virtual-source responses retrieved through the application of SI by CC suffers from irregularities in the illumination pattern (Tsai 2009; Weaver *et al.* 2009). In this section, we use the theory described in Section 2.4 to extract Rayleigh-wave dispersion curves from virtual-source responses obtained through the application of SI by CC and SI by MDD. The extracted dispersion curves are then compared to those obtained from the matched-field processing (e.g. Baggeroer *et al.* 1993) described in Section 2.5.

To extract discrete phase velocities, we use the spectra of the virtual-source responses retrieved through the application of SI by CC and SI by MDD [i.e. $\hat{C}(\boldsymbol{x}_\mathrm{R}, \boldsymbol{x})$ and $\hat{\tilde{G}}_\mathrm{d}^{(\mathrm{a})}(\boldsymbol{x}_\mathrm{R}, \boldsymbol{x}')$, respectively]. In practice, a set of phase velocities for discrete values of ω_j, that is, the zero-crossings of the real (and imaginary) part of the virtual-source responses, is given by $\hat{c}_n = \omega_j \left|\boldsymbol{x}_\mathrm{R} - \boldsymbol{x}\right| / z_n$, where z_n with ($n = 1$, 2, ...) are the known zeros of the appropriate analytical function. As described in Section 2.4, we use the zero-crossings of J_0 and $-Y_1$ for the real parts of $\hat{C}\left(\boldsymbol{x}_\mathrm{R}, \boldsymbol{x}\right)$ and $\hat{\tilde{G}}_\mathrm{d}^{(\mathrm{a})}\left(\boldsymbol{x}_\mathrm{R}, \boldsymbol{x}'\right)$, respectively. Since we consider a one-sided illumination, we may also extract discrete phase velocity values from the imaginary parts of $\hat{C}\left(\boldsymbol{x}_\mathrm{R}, \boldsymbol{x}\right)$ and $\hat{\tilde{G}}_\mathrm{d}^{(\mathrm{a})}\left(\boldsymbol{x}_\mathrm{R}, \boldsymbol{x}'\right)$. For this purpose, we use the zeros of $-\boldsymbol{H}_0$ and $-J_1$, respectively (see Section 2.4).

We consider different combinations of ω_j and z_n and choose the most plausible phase velocity value for each ω_j (Fig. 10). Here, we define plausible as closest to the reference dispersion curve, which is the constant acoustic velocity (1650 m s^{-1}) for the synthetic data and the dispersion curve obtained from matched-field processing for the field data. The latter is obtained by applying matched-field processing to data from single shots recorded across the array. In particular, we calculate the discrete phase velocity values forming the dispersion curve by averaging over 8 Hz wide frequency bands (in 0.2 Hz steps) with 50 per cent overlap. This results in phase velocity values every 4 Hz, where each value is obtained by averaging over 8 Hz / 0.2 Hz = 40 matched-field processing results (see eq. 15). Because the locations of the hammer blows are known, we only need to search for the best matching phase velocity in each frequency band of consideration. The final dispersion curve depicted in Fig. 10 is the average of curves obtained from several hammer blows. To avoid spatial aliasing, we use two additional receivers for matched-field processing, which are not shown in Fig. 2. Both receivers were separated by about 1 m from the centre receiver forming a short line parallel to the long receiver lines. All presented dispersion curves in this section are obtained by processing data from 76 regularly spaced sources.

Fig. 10 shows a similar picture for synthetic and glacier data: Whereas high frequency phase velocities ($\gtrapprox$ 100 Hz) extracted from SI by CC and SI by MDD responses are very similar (for glacier data only 'picked' up to 170 Hz due to non-smoothness at higher frequencies which is most likely caused by reduced energy in this band), SI by CC yields lower phase velocity values than SI by MDD for low frequencies ($\lessapprox$100 Hz). In this part, SI by MDD phase velocity estimates are generally closer to the reference dispersion curves than those obtained from SI by CC. This again suggests that medium responses retrieved through SI by MDD are less affected by a non-uniform illumination pattern compared to medium responses retrieved through SI by CC. As was the case in the monitoring application, we expect that this difference in performance between SI by CC and SI by MDD will be even more significant for a reduced number of sources. Nevertheless, for interstation distances smaller

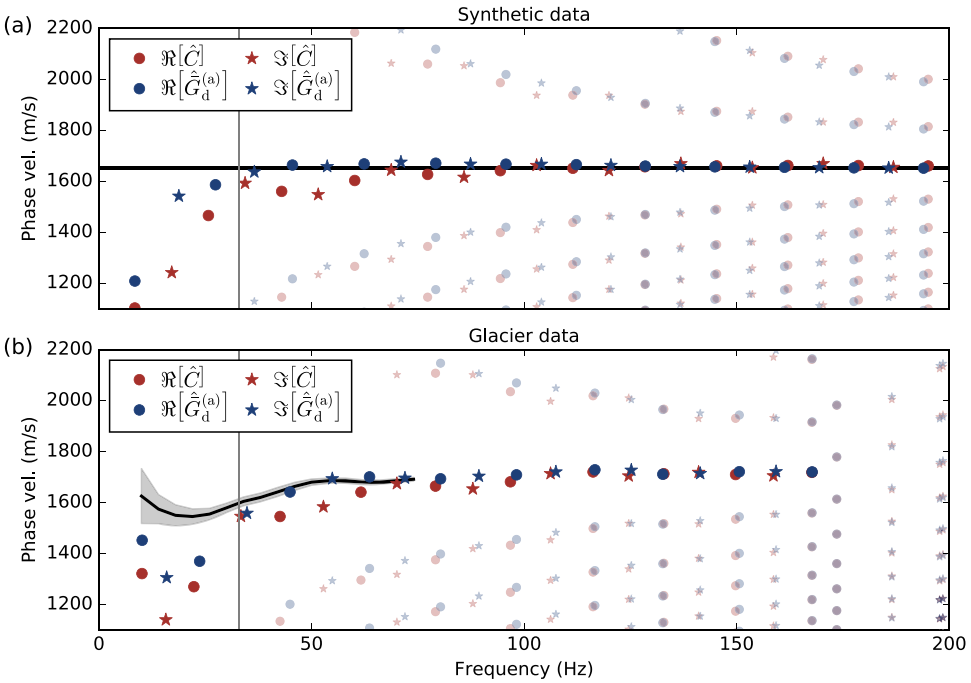

Figure 10. Discrete phase velocity values derived from zero crossings of real and imaginary parts of SI by CC ($\hat{C}(\boldsymbol{x}_\mathrm{R}, \boldsymbol{x})$) and SI by MDD ($\hat{\tilde{G}}_\mathrm{d}^{(\mathrm{a})}(\boldsymbol{x}_\mathrm{R}, \boldsymbol{x}')$) response spectra (see the text for details). Large solid symbols are considered the seismologically most plausible values; small transparent symbols are discarded. The grey vertical line indicates the frequency at which the interstation distance is (approximately) equal to a wavelength. (a) Synthetic data; the black horizontal line indicates the homogeneous acoustic medium velocity of 1650 m s^{-1}. (b) Glacier data; the black horizontal line is the average dispersion curve derived from matched-field processing applied to single hammer blows. The shaded area around it indicates one standard deviation.

than the wavelength ($\lessapprox$33 Hz), both SI by CC and SI by MDD phase velocities are strongly underestimated.

Interestingly, both the Bessel function approach and matched-field processing find a local minimum in the field data phase velocity dispersion curve at around 15–20 Hz. Qualitatively, this suggests the presence of a low velocity layer in the interior of the glacier or at the glacier base. A detailed discussion about this observation is beyond the scope of this work but may have interesting implications for englacial properties.

7 CONCLUSION

This study investigates the applicability of two alternative interferometric techniques for the purpose of englacial monitoring. As such, we successfully retrieved virtual-source medium responses by applying SI by MDD and VRS to both synthetic data and field data from a glacier. Both techniques have proven successful in correcting the phase distortions of SI by CC responses introduced by non-uniform illumination patterns through a multidimensional deconvolution process. Compared to SI by CC, this implies that the accuracy of velocity variation estimates is increased. Additionally, the emergence of virtual reflections through the application of VRS making up for the lack of natural coda allows even more accurate measurements of small relative velocity variations. With respect to phase velocity extraction, SI by MDD results are superior to SI by CC results, which will improve the quality of tomographic images derived from these data.

In summary, the results of this study demonstrate the potential of VRS for monitoring applications in glacial settings. This is promising since the low-scattering properties of ice bodies complicate the application of CWI. Furthermore, the reflection coda obtained through the application of VRS virtually enlarges the array aperture, which is beneficial for small-scale glacial applications which tend to yield short traveltimes of direct waves through monitoring arrays. Furthermore, time- and space-dependent icequake source locations are another motivation for using multidimensional deconvolution techniques. From a practical point of view, the increased number of receivers needed for these techniques (compared to SI by CC) might seem problematic at a first glance. However, recent advances in instrumentation have allowed first deployments of large-N arrays in glacial settings (Bartholomaus *et al.* 2017; Labedz *et al.* 2017). Comprising a dense deployment of a large number of receivers, such large-N arrays provide the requirements (i.e. receiver contours) for SI by MDD and VRS, thus opening up the opportunity for the application of these methods to field data on a larger scale.

ACKNOWLEDGEMENTS

This work was funded by the Swiss National Science Foundation project Glacial Hazard Monitoring with Seismology (GlaHMSeis project PP00P2_157551). CH acknowledges support from the Emmy Noether program (HA7019/1-1) of the German Research Foundation (DFG). We thank Hansruedi Maurer and his group for providing seismic equipment; additional instrumentation was provided by the Geophysical Instrument Pool of the German Research Centre for Geosciences (project AnICEotropy). The authors would like to thank Editor Wolfgang Friederich as well as an anonymous reviewer and Dylan Mikesell for their valuable comments. Furthermore, we gratefully acknowledge support in the field from Christian Böhm, Florent Gimbert, Gabi Laske, Lukas Preiswerk, Korbinian Sager, Julien Seguinot and Cornelius Senn. Jan Thorbecke provided valuable support in creating the synthetic data. This paper is based upon work from COST Action ES1401-TIDES, supported

by COST (European Cooperation in Science and Technology). We used Python and the ObsPy package (Beyreuther *et al.* 2010) for data processing. The figures were created using the Matplotlib plotting library for Python (Hunter 2007) and the QGIS Open Source Geographic Information System.

FL processed the data and the results were analysed by FL with assistence of "CW" (co-author Cornelis Weemstra, CW), FW and CH. Major parts of the manuscript were written by FL with contributions from CW, FW and CH. The theory section was written by CW with contributions from FL, FW and CH.

REFERENCES

Aki, K., 1957. Space and time spectra of stationary stochastic waves, with special reference to microtremors., *Bull. Earthq. Res. Inst. Uni. Tokyo,* **35,** 415–457.

Aki, K. & Chouet, B., 1975. Origin of coda waves: source, attenuation, and scattering effects, *J. geophys. Res.,* **80**(23), 3322–3342.

Aki, K. & Richards, P.G., 2002. *Quantitative Seismology,* 2nd edn, University Science Books.

Amundson, J.M., Truffer, M., Lüthi, M.P., Fahnestock, M., West, M. & Motyka, R.J., 2008. Glacier, fjord, and seismic response to recent large calving events, Jakobshavn Isbræ, Greenland, *Geophys. Res. Lett.,* **35**(22), L22501.

Arfken, G.B. & Weber, H.J., 2005. *Mathematical Methods for Physicists,* 6th edn, Elsevier Academic Press.

Baggeroer, A., Kuperman, W. & Mikhalevsky, P., 1993. An overview of matched field methods in ocean acoustics, *IEEE J. Ocean. Eng.,* **18**(4), 401–424.

Bakulin, A. & Calvert, R., 2006. The virtual source method: theory and case study, *Geophysics,* **71**(4), SI139–SI150.

Bartholomaus, T.C., Labedz, C.R., Amundson, J.M., Gimbert, F., Tsai, V.C., Vore, M.E. & Karplus, M.S., 2017. Spatio-temporal evolution of efficient subglacial water discharge at Lemon Creek Glacier, Alaska, *Abstract (C41D-1270) presented at 2017 AGU Fall Meeting,* American Geophysical Union.

Bassis, J.N., Fricker, H.A., Coleman, R. & Minster, J.-B., 2008. An investigation into the forces that drive ice-shelf rift propagation on the Amery Ice Shelf, East Antarctica, *J. Glaciol.,* **54**(184), 17–27.

Bender, C.M. & Orszag, S.A., 2013. *Advanced Mathematical Methods for Scientists and Engineers I: Asymptotic Methods and Perturbation Theory,* Springer-Verlag.

Benn, D.I., Warren, C.R. & Mottram, R.H., 2007. Calving processes and the dynamics of calving glaciers, *Earth-Sci. Rev.,* **82,** 143–179.

Beyreuther, M., Barsch, R., Krischer, L., Megies, T., Behr, Y. & Wassermann, J., 2010. Obspy: a Python toolbox for seismology, *Seismol. Res. Lett.,* **81**(3), 530–533.

Boschi, L. & Weemstra, C., 2015. Stationary-phase integrals in the cross-correlation of ambient noise, *Rev. Geophys.,* **53,** 411–451.

Boschi, L., Weemstra, C., Verbeke, J., Ekstrom, G., Zunino, A. & Giardini, D., 2013. On measuring surface wave phase velocity from station-station cross-correlation of ambient signal, *Geophys. J. Int.,* **192,** 346–358.

Brenguier, F., Shapiro, N.M., Campillo, M., Ferrazzini, V., Duputel, Z., Coutant, O. & Nercessian, A., 2008. Towards forecasting volcanic eruptions using seismic noise, *Nat. Geosci.,* **1**(2), 126–130.

Campillo, M., 2003. Long-range correlations in the diffuse seismic coda, *Science,* **299**(5606), 547–549.

Chang, J.P., Ridder, S. A. L.D. & Biondi, B.L., 2016. High-frequency Rayleigh-wave tomography using traffic noise from Long Beach, California, *Geophysics,* **81**(2), B1–B11.

Clarke, D., Zaccarelli, L., Shapiro, N.M. & Brenguier, F., 2011. Assessment of resolution and accuracy of the moving window cross spectral technique for monitoring crustal temporal variations using ambient seismic noise, *Geophys. J. Int.,* **186**(2), 867–882.

Clarke, G.K., 2005. Subglacial processes, *Annu. Rev. Earth Planet. Sci.,* **33**(1), 247–276.

Colgan, W., Rajaram, H., Abdalati, W., McCutchan, C., Mottram, R., Moussavi, M.S. & Grigsby, S., 2016. Glacier crevasses: observations, models, and mass balance implications, *Rev. Geophys.,* **54** (1), 119–161.

Colombi, A., Chaput, J., Brenguier, F., Hillers, G., Roux, P. & Campillo, M., 2014. On the temporal stability of the coda of ambient noise correlations, *C. R. Geosci.,* **346**(11–12), 307–316.

Corciulo, M., Roux, P., Campillo, M., Dubucq, D. & Kuperman, W.A., 2012. Multiscale matched-field processing for noise-source localization in exploration geophysics, *Geophysics,* **77**(5), KS33–KS41.

Dalen, K. N.V., Mikesell, T.D., Ruigrok, E.N. & Wapenaar, K., 2015. Retrieving surface waves from ambient seismic noise using seismic interferometry by multidimensional deconvolution, *J. Geophys. Res.,* (120), 944–961.

Das, S.B., Joughin, I., Behn, M.D., Howat, I.M., King, M.A., Lizarralde, D. & Bhatia, M.P., 2008. Fracture propagation to the base of the Greenland ice sheet during supraglacial lake drainage, *Science,* **1,** 778–781.

Deichmann, N. & Röthlisberger, H., 1979. Observations of glacier seismicity on Unteraargletscher, *J. Glaciol.,* **23**(89), 409.

Ekström, G., Abers, G. & Webb, S., 2009. Determination of surface-wave phase velocities across USArray from noise and Aki's spectral formulation, *Geophys. Res. Lett.,* **36**(18), doi:10.1029/2009GL039131.

Fountain, A.G. & Walder, J.S., 1998. Water flow through temperate glaciers, *Rev. Geophys.,* **36**(97), 299–328.

Fricker, H.A., Young, N.W., Coleman, R., Bassis, J.N. & Minster, J.-B., 2005. Multi-year monitoring of rift propagation on the Amery Ice Shelf, East Antarctica, *Geophys. Res. Lett.,* **32**(2), L02502, doi:10.1029/2004GL021036

Froment, B., Campillo, M., Roux, P., Gouédard, P., Verdel, A. & Weaver, R.L., 2010. Estimation of the effect of nonisotropically distributed energy on the apparent arrival time in correlations, *Geophysics,* **75**(5), SA85–SA93.

Gouedard, P. *et al.*, 2008. Cross-correlation of random fields: mathematical approach and applications, *Geophys. Prospect.,* **56**(3), 375–393.

Grêt, A., Snieder, R. & Scales, J., 2006. Time-lapse monitoring of rock properties with coda wave interferometry, *J. geophys. Res.,* **111**(B3), B03305, doi:10.1029/2004JB003354.

Hadziioannou, C., Larose, E., Coutant, O., Roux, P. & Campillo, M., 2009. Stability of monitoring weak changes in multiply scattering media with ambient noise correlation: laboratory experiments., *J. acoust. Soc. Am.,* **125**(6), 3688–95.

Halliday, D. & Curtis, A., 2008. Seismic interferometry, surface waves and source distribution, *Geophys. J. Int.,* **175**(3), 1067–1087.

Halliday, D., Curtis, A. & Kragh, E., 2008. Seismic surface waves in a suburban environment: active and passive interferometric methods, *Leading Edge,* **27,** 210–128.

Huggel, C., Zgraggen-Oswald, S., Haeberli, W., Kääb, A., Polkvoj, A., Galushkin, I. & Evans, S.G., 2005. The 2002 rock/ice avalanche at Kolka/Karmadon, Russian Caucasus: assessment of extraordinary avalanche formation and mobility, and application of QuickBird satellite imagery, *Nat. Hazards Earth Syst. Sci.,* **5**(2), 173–187.

Hulbe, C. & Fahnestock, M., 2003. Climate-induced ice shelf disintegration in the Antarctic peninsula, in *Antarctic Peninsula Climate Variability: Historical and Paleoenvironmental Perspectives,* pp. 79–92, eds Domack, E., Leventer, A., Burnett, A., Bindschadler, R.A., Convey, P. & Kirby, M., American Geophysical Union.

Hunter, J.D., 2007. Matplotlib: a 2D graphics environment, *Comput. Sci. Eng.,* **9**(3), 90–95.

Hunziker, J., van der Neut, J., Slob, E. & Wapenaar, K., 2009. Controlled source interferometry with noisy data, in *SEG Technical Program Expanded Abstracts,* pp. 689–693, Society of Exploration Geophysicists.

Huss, M., Voinesco, A. & Hoelzle, M., 2013. Implications of climate change on Glacier de la Plaine Morte, Switzerland, *Geogr. Helv.,* **68**(4), 227–237.

Iken, A. & Bindschadler, R.A., 1986. Combined measurements of subglacial water pressure and surface velocity of Findelengletscher, Switzerland: conclusions about drainage system and sliding mechanism, *J. Glaciol.,* **32**(110), 101–119.

Jain, S.K., Lohani, A.K., Singh, R.D., Chaudhary, A. & Thakural, L.N., 2012. Glacial lakes and glacial lake outburst flood in a Himalayan basin using remote sensing and GIS, *Nat. Hazards,* **62**(3), 887–899.

Joughin, I. & MacAyeal, D.R., 2005. Calving of large tabular icebergs from ice shelf rift systems, *Geophys. Res. Lett.,* **32**(2).

Kimman, W.P. & Trampert, J., 2010. Approximations in seismic interferometry and their effects on surface waves, *Geophys. J. Int.,* **182**(1), 461–476.

Labedz, C.R., Bartholomaus, T.C., Gimbert, F., Amundson, J.M., Vore, M.E., Karplus, M.S. & Tsai, V.C., 2017. Seismic observations of subglacial water discharge from glacier-dammed lake drainage at Lemon Creek Glacier, Alaska, *Abstract (C41D-1267) presented at 2017 AGU Fall Meeting, 11-15 Dec,* American Geophysical Union.

Lawrence, W.S. & Qamar, a., 1979. Hydraulic transients: a seismic source in volcanoes and glaciers., *Science,* **203**(4381), 654–656.

Lecocq, T., Caudron, C. & Brenguier, F., 2014. MSNoise, a Python package for monitoring seismic velocity changes using ambient seismic noise, *Seismol. Res. Lett.,* **85**(3), 715–726.

Lehujeur, M., , Vergne, J., Schmittbuhl, J. & Maggi, A., 2015. Characterization of ambient seismic noise near a deep geothermal reservoir and implications for interferometric methods: a case study in northern Alsace, France, *Geotherm. Energy,* **3**(3), doi:10.1186/s40517-014-0020-2.

Lobkis, O.I. & Weaver, R.L., 2003. Coda-wave interferometry in finite solids: recovery of P-to-S conversion rates in an elastodynamic billiard, *Phys. Rev. Lett.,* **90**(25), doi:10.1103/PhysRevLett.90.254302.

Mikesell, T.D., Van Wijk, K., Haney, M.M., Bradford, J.H., Marshall, H.P. & Harper, J.T., 2012. Monitoring glacier surface seismicity in time and space using Rayleigh waves, *J. geophys. Res.,* **117**(2), 1–12.

Minato, S., Matsuoka, T., Tsuji, T., Draganov, D., Hunziker, J. & Wapenaar, K., 2011. Seismic interferometry using multidimensional deconvolution and crosscorrelation for crosswell sesimic reflection data without borehole sources, *Geophysics,* **76,** SA19–SA34.

Mordret, A., Mikesell, T.D., Harig, C., Lipovsky, B.P. & Prieto, A., 2016. Monitoring southwest Greenland's ice sheet melt with ambient seismic noise, *Sci. Adv.,* **2,** 1–11.

Neave, K.G. & Savage, J.C., 1970. Icequakes on the Athabasca Glacier, *J. geophys. Res.,* **75**(8), 1351–1362.

Obermann, A., Froment, B., Campillo, M., Larose, E., Planès, T., Valette, B., Chen, J.H. & Liu, Q.Y., 2014. Seismic noise correlations to image structural and mechanical changes associated with the M_w 7.9 2008 Wenchuan earthquake, *J. geophys. Res.,* **119,** 3155–3168.

Phillips, T., Rajaram, H. & Steffen, K., 2010. Cryo-hydrologic warming: a potential mechanism for rapid thermal response of ice sheets, *Geophys. Res. Lett.,* **37,** doi:10.1029/2010GL044397.

Podolskiy, E. & Walter, F., 2016. Cryoseismology, *Rev. Geophys.,* **54,** 708–758.

Poletto, F. & Bellezza, C., 2012. Multidimensional deconvolution of seismic-interferometry Arctic data, in *SEG Technical Program Expanded Abstracts,* **31,** pp. 1–5 , Society of Exploration Geophysicists.

Poupinet, G., Ellsworth, W. & Frechet, J., 1984. Monitoring velocity variations in the crust using earthquake doublets: an application to the Calaveras Fault, California, *J. geophys. Res.,* **89**(B7), 5719–5731.

Pralong, A. & Funk, M., 2005. Dynamic damage model of crevasse opening and application to glacier calving, *J. geophys. Res.,* **110,** doi:10.1029/2004JB003104.

Ratdomopurbo, A. & Poupinet, G., 1995. Monitoring a temporal change of seismic velocity in a volcano: application to the 1992 eruption of Mt. Merapi (Indonesia), *Geophys. Res. Lett.,* **22**(7), 775–778.

Richardson, S.D. & Reynolds, J.M., 2000. An overview of glacial hazards in the Himalayas, *Quat. Int.,* **65-66,** 31–47.

Roberts, M.J., 2005. Jökulhlaups: a reassessment of floodwater flow through glaciers, *Rev. Geophys.,* **43**(1), 1–21.

Rott, H., Skvarca, P. & Nagler, T., 1996. Rapid collapse of northern Larsen ice shelf, Antarctica, *Science,* **271**(5250), 788–792.

Roux, P.F., Walter, F., Riesen, P., Sugiyama, S. & Funk, M., 2010. Observation of surface seismic activity changes of an Alpine glacier during a glacier-dammed lake outburst, *J. geophys. Res.,* **115**(3), 1–13.

Scambos, T., Hulbe, C. & Fahnestock, M., 2003. Climate-induced ice shelf disintegration in the Antarctic peninsula. Antarctic Peninsula Climate Variability: Historical and Paleoenvironmental Perspectives, 79–92.

Schuster, G.T., Yu, J., Sheng, J. & Rickett, J., 2004. Interferometric/daylight seismic imaging, *Geophys. J. Int.,* **157**(2), 838–852.

Sens-Schönfelder, C. & Wegler, U., 2006. Passive image interferemetry and seasonal variations of seismic velocities at Merapi Volcano, Indonesia, *Geophys. Res. Lett.,* **33**(21), L21302, doi:10.1029/2006GL027797.

Shapiro, N.M. & Campillo, M., 2004. Emergence of broadband Rayleigh waves from correlations of the ambient seismic noise, *Geophys. Res. Lett.,* **31**(7), L07614, doi:10.1029/2004GL019491.

Snieder, R., 2004. Extracting the Green's function from the correlation of coda waves: a derivation based on stationary phase, *Phys. Rev. E,* **69**(4), doi:10.1103/PhysRevE.69.046610.

Snieder, R., Grêt, A., Douma, H. & Scales, J., 2002. Coda wave interferometry for estimating nonlinear behavior in seismic velocity, *Science ,* **295**(5563), 2253–2255.

Snieder, R., van Wijk, K., Haney, M. & Calvert, R., 2008. Cancellation of spurious arrivals in Green's function extraction and the generalized optical theorem, *Phys. Rev. E,* **78**(3), doi:10.1103/PhysRevE.78.036606.

Thorbecke, J.W. & Draganov, D., 2011. Finite-difference modeling experiments for seismic interferometry, *Geophysics,* **76**(6), H1–H18.

Tsai, V.C., 2009. On establishing the accuracy of noise tomography traveltime measurements in a realistic medium, *Geophys. J. Int.,* **178**(3), 1555–1564.

Tsai, V.C., 2011. Understanding the amplitudes of noise correlation measurements, *J. geophys. Res.,* **116**(B09), B09311, doi:10.1029/2011JB008483.

Tsai, V.C. & Moschetti, M.P., 2010. An explicit relationship between time-domain noise correlation and spatial autocorrelation (SPAC) results, *Geophys. J. Int.,* **182**(1), 454–460.

van Dalen, K.N., Mikesell, T.D., Ruigrok, E.N. & Wapenaar, K., 2015. Retrieving surface waves from ambient seismic noise using seismic interferometry by multidimensional deconvolution, *J. geophys. Res.,* **120,** 944–961.

van Dalen, K.N., Wapenaar, K. & Halliday, D.F., 2014. Surface wave retrieval in layered media using seismic interferometry by multidimensional deconvolution, *Geophys. J. Int.,* **196,** 230–242.

van der Neut, J., 2012. Interferometric redatuming by multidimensional deconvolution, *PhD thesis*, Delft University of Technology.

van der Neut, J., Thorbecke, J., Mehta, K., Slob, E. & Wapenaar, K., 2011. Controlled-source interferometric redatuming by crosscorrelation and multidimensional deconvolution in elastic media, *Geophysics,* **76**(4), SA63–SA76.

Van der Veen, C., 1998. Fracture mechanics approach to penetration of surface crevasses on glaciers, *Cold Reg. Sci. Technol.,* **27**(1), 31–47.

van Wijk, K., Mikesell, T.D., Schulte-Pelkum, V. & Stachnik, J., 2011. Estimating the Rayleigh-wave impulse response between seismic stations with the cross terms of the Green tensor, *Geophys. Res. Lett.,* **38**(16), L16301.

Walter, F., Clinton, J.F., Deichmann, N., Dreger, D.S., Minson, S.E. & Funk, M., 2009. Moment tensor inversions of icequakes on Gornergletscher, Switzerland, *Bull. seism. Soc. Am.,* **99**(212), 3–33.

Walter, F., Roux, P., Roeoesli, C., Lecointre, A., Kilb, D. & Roux, P.F., 2015. Using glacier seismicity for phase velocity measurements and Green's function retrieval, *Geophys. J. Int.,* **201**(3), 1722–1737.

Wapenaar, K. & Fokkema, J., 2006. Green's function representations for seismic interferometry, *Geophysics,* **71**(4), SI33–SI46.

Wapenaar, K., Ruigrok, E., van der Neut, J. & Draganov, D., 2011a. Improved surface-wave retrieval from ambient seismic noise by multi-dimensional deconvolution, *Geophys. Res. Lett.,* **38**(1), L01313, doi:10.1029/2010GL045523.

Wapenaar, K. & van der Neut, J., 2010. A representation for Green's function retrieval by multidimensional deconvolution, *J. acoust. Soc. Am.,* **128**(6), EL366–EL371.

Wapenaar, K., van der Neut, J., Ruigrok, E., Draganov, D., Hunziker, J., Slob, E., Thorbecke, J. & Snieder, R., 2011b. Seismic interferometry by crosscorrelation and by multidimensional deconvolution: a systematic comparison, *Geophys. J. Int.,* **185**(3), 1335–1364.

Weaver, R., Froment, B. & Campillo, M., 2009. On the correlation of non-isotropically distributed ballistic scalar diffuse waves., *J. acoust. Soc. Am.,* **126**(4), 1817–1826.

Weemstra, C., Boschi, L., Goertz, A. & Artman, B., 2013. Seismic attenuation from recordings of ambient noise, *Geophysics,* **78**(1), Q1–Q14.

Weemstra, C., Draganov, D., Ruigrok, E.N., Hunziker, J., Gomez, M. & Wapenaar, K., 2017a. Application of seismic interferometry by multidimensional deconvolution to ambient seismic noise recorded in Malargüe, Argentina, *Geophys. J. Int.,* **208**(2), 693–714.

Weemstra, C., Obermann, A., Verdel, A., Paap, B., Blanck, H., Gunason, E.Á., Hersir, G.P., Jousset, P. & Sigurdsson, Ó., 2016. Time-lapse seismic imaging of the Reykjanes geothermal reservoir, in *Proceedings of the European Geotherm. Congr.,* Strasbourg, France, paper #207.

Weemstra, C., Snieder, R. & Boschi, L., 2015a. On the estimation of attenuation from the ambient seismic field: inferences from distributions of isotropic point scatterers, *Geophys. J. Int.,* **203,** 1054–1071.

Weemstra , C., Wapenaar, K. & Van Dalen , K.N., 2015b. Reflecting boundary conditions for interferometry by multidimensional deconvolution. *SEG Technical Program Expanded Abstracts,* Vol. **34,** Society of Exploration Geophysicists, pp. 2440–2444.

Weemstra, C., Wapenaar, K. & van Dalen, K.N., 2017b. Reflecting boundary conditions for interferometry by multidimensional deconvolution, *J. acoust. Soc. Am.,* **142**(4), 2242–2257.

Weemstra, C., Westra, W., Snieder, R. & Boschi, L., 2014. On estimating attenuation from the amplitude of the spectrally whitened ambient seismic field, *Geophys. J. Int.,* **197,** 1770–1788.

Xu, Z. & Mikesell, T.D., 2017. On the reliability of direct rayleigh-wave estimation from multicomponent cross-correlations, *Geophys. J. Int.,* **210**(3), 1388–1393.

Yang, Y. & Ritzwoller, M.H., 2008. Characteristics of ambient seismic noise as a source for surface wave tomography, *Geochem. Geophys. Geosyst.,* **9**(2), Q02008, doi:10.1029/2007GC001814.

Yao, H. & van der Hilst, R.D., 2009. Analysis of ambient noise energy distribution and phase velocity bias in ambient noise tomography, with application to SE Tibet, *Geophys. J. Int.,* **179**(2), 1113–1132.

Yao, H., van der Hilst, R.D. & de Hoop, M.V., 2006. Surface-wave array tomography in SE Tibet from ambient seismic noise and two-station analysis—I. Phase velocity maps, *Geophys. J. Int.,* **166,** 732–744.

Zhan, Z., Tsai, V.C. & Clayton, R.W., 2013. Spurious velocity changes caused by temporal variations in ambient noise frequency content, *Geophys. J. Int.,* **194**(3), 1574–1581.